High resolution modeling of aluminium transport in a fjord estuary with focus on mean circulation and irregular flow events

Magne Simonsen [a,b,*], Jon Albretsen [c], Øyvind Saetra [a], Lars Asplin [c], Ole Christian Lind [b], Hans-Christian Teien [b]

[a] Norwegian Meteorological Institute, P.O. Box 43, Blindern, NO-0313 Oslo, Norway
[b] Centre of Environmental Radioactivity CoE, Faculty of Environmental Sciences and Natural Resource Management, Norwegian University of Life Sciences (NMBU), P.O. Box 5003, NO-1433 Ås, Norway
[c] Institute of Marine Research, P.O. Box 1870, Nordnes, NO-5817 Bergen, Norway

HIGHLIGHTS

- Small-scale dynamics are usually not included in transport model estimates.
- Here, estuarine and fjord contaminant transport was modeled at high detail level.
- Model results agree well with observed Al concentrations and hydrographic profiles.
- Model results show scattered concentrations with high variability.
- Wind-induced reversed flow events can deviate significantly from normal conditions.

GRAPHICAL ABSTRACT
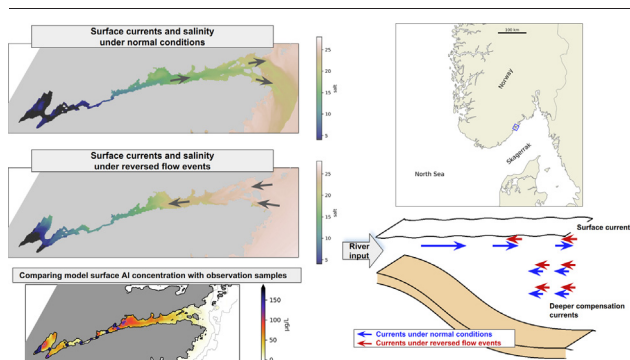
ARTICLE INFO

Editor: Prof. Ashantha Goonetilleke

ABSTRACT

Environmental impact assessments of trace metals and radionuclides in estuarine waters will benefit from numerical transport models that can provide detailed and accurate predictions of concentrations of harmful physico-chemical forms of contaminants at adequate spatial and temporal resolution. Aiming to study the potential of aluminium (Al) exposure to biota, a transport model (OpenDrift) including dynamic speciation and transformation processes was improved and applied, using three-dimensional hydrodynamic flow fields from a numerical ocean model (ROMS) at high horizontal resolution (32 m). Al transport and concentration was computed along the Sandnesfjorden Fjord, southeastern Norway, from river outlet to open coastal waters. Validation of the circulation model with 29 hydrographic profiles from Sandnesfjorden showed substantial improvements compared to previous studies due to optimized model configuration (salinity overestimation decreased from >7 psu to <4 psu). Modeled Al data compared well with observed surface Al concentration from 12 locations and the along-fjord decreasing trend in Al-concentration was well reproduced (error ratios were <2 in Sandnesfjorden). Except in the channel area, both salinity and Al concentration estimates lie well within the expected variability. However, the transport modeling gave a more detailed site-specific picture of the Al concentration, suggesting more scattered and variable fields than indicated by observational data (variations of a factor 3–4 over short spatiotemporal scales). Reversed flow events (surface flow into the fjord) caused considerable mixing and redistribution of water masses, affecting both horizontal mixing of river discharges with coastal water as well as vertically as surface water mixed with deeper water masses. These blocking events strongly changed properties and distribution of the water masses giving rise to local and short-term high Al-exposure episodes (variations of a factor of 10 over a 12 h period) in the fjord that may pose risks to biota and therefore should be taken into account in impact and risk assessments.

* Corresponding author at: Norwegian Meteorological Institute, P.O. Box 43, Blindern, NO-0313 Oslo, Norway.
  E-mail address: magnes@met.no (M. Simonsen).

1. Introduction

Estuaries are marine zones where fresh water from rivers mixes with the saline coastal water. These are strongly dynamic active regions characterized by strong gradients, comprising the interface between inland and coastal waters, and are important for sediment formation, biological production and distribution of contaminants (Syvitski et al., 1987; Hobbie, 2000). In aquatic and marine environments, trace metals can be present in a series of different physico-chemical forms (species), such as low molecular mass (LMM) species, polymers, humic colloids and particle- or sediment bound species. On their way through the estuaries, the distribution of species (speciation) is affected by a number of complex physical and chemical transformation processes, such as sorption, remobilization, polymerization, aggregation, sedimentation and resuspension, initiated by shifting environmental conditions such as pH, salinity and temperature, as observed and described by studies from a range of different study sites (Hydes and Liss, 1977; Teien et al., 2004; Upadhyay, 2008; Wang et al., 2015; Tipping et al., 2016; Jones et al., 2019; Liu et al., 2022).

The value of model estimates of contaminant transport in estuarine and coastal environments with salinity intervals ranging from pure fresh water near the river outlet to saline offshore water depends on the complexity and detail level in the descriptions of processes solved by the model and hence on the uncertainties attributed to the model results. Relevant factors affecting the overall uncertainties of such numerical model predictions can be the spatio-temporal scale of hydrodynamical currents (ocean state), details regarding the description of the source term and release scenario as well as model assumptions regarding the biogeochemical processes taking place (Ganju et al., 2016; Salbu, 2016). Hence, a model system that is able to estimate detailed spatio-temporal variations of the different physico-chemical forms of a contaminant may potentially provide new essential knowledge about the downstream consequences (environmental and human health issues as well as sociological and economical aspects) caused by natural processes and anthropogenic activities (e.g., road run-off, mining, river liming and aquaculture). Both historical analyses and up-to-date predictions of contaminant exposure to biota are therefore of the highest relevance for environmental management and monitoring since it ultimately can feed into impact and risk assessment models (Machado et al., 2016). According to Machado et al. (2016), one of the remaining challenges regarding metal behavior and toxicity in estuaries is to develop more robust conceptual and quantitative models for detailed prediction of contaminant exposure to biota, taking the complexity of different spatio-temporal scales into account. Therefore, to be able to estimate metal concentrations through an estuary, the circulation must be resolved at sufficiently high resolution, while all relevant physico-chemical transformation processes for metal speciation should be implemented in the transport model (Ganju et al., 2016).

An example of a river-borne contaminant is aluminium (Al), which may undergo transformation to acute toxic species for salmonid fish as a result of chemical processes in estuaries (Teien et al., 2006). Like other metals, the transport properties will depend on the speciation, as LMM and colloidal species are transported passively with the water masses, while the larger particle-bound species will sink and settle in the seabed sediments, where they subsequently may be subject to resuspension or remobilization.

Several studies have modeled and monitored the global scale transport of Al (e.g., Resing et al., 2015; Artigue et al., 2021; Xu and Weber, 2021), although at coarse spatial resolution. To resolve the estuarine circulation, high-resolution numerical ocean models can capture much of the small scale hydrodynamics. However, increasing the model resolution to a sufficient level has a computational cost and the unresolved turbulent transport at sub-grid scales must still be described by parameterizations. Different approaches have previously been employed, using structured as well as unstructured grids at horizontal resolutions from 10 m up to km scale (e.g., Arndt et al., 2007; Chao et al., 2017; Ivanov et al., 2020). Applications of depth-integrated two dimensional currents (e.g., Arndt et al., 2007; Bars et al., 2016) or fully three dimensional hydrodynamics (Yang and Khangaonkar, 2009; Vallaeys et al., 2021) have been studied. The transport of sediments, nutrients, trace metals and contaminants in estuaries has

previously, among others, been described by Hartnett and Berry (2012); Elskens et al. (2014); Zhou et al. (2017), but to our knowledge, no one has simulated estuarine metal transport including speciation using three dimensional hydrodynamic fields at horizontal resolution higher than 32 m as applied by (Simonsen et al., 2019b).

With the overall goal of reducing model uncertainties, we have here developed and applied a numerical model system with the capability to describe and predict contaminant transport and concentration levels through the estuarine mixing zone. Aiming for an environmental description being as correct as possible, our model system has a high detail level, both regarding spatio-temporal resolution as well as considering all relevant interactions and transformation processes taking place. As a realistic case study, we have investigated some important aspects of applying the high-resolution hydrodynamic model to estimate the Al transport in Sandnesfjorden in southern Norway (Fig. 1) during the summer season 2019. The site is the same as that studied by Simonsen et al., (2019b), who suggested vertical stratification and flow through the basins near the river outlet as issues to be addressed for further improvement. Hence, we have here taken specific measures to refine the hydrodynamic simulation. For other applications, our generic model system may also be capable of modeling cases involving any radionuclide or trace metal released into the coastal marine environment, utilizing generic or site-specific elemental parameters.

The main aim of the present study is to demonstrate how the relevant model improvements for the case study of Al transport in Sandnesfjorden during the summer season 2019 were able to produce detailed features in the flow field that can be important for the prediction of potential Al exposure to marine organisms. To achieve this, we set out to address the following objectives: i) to evaluate the hydrodynamic model data with respect to hydrography, mean flow and reversed flow events; ii) to assess the Al transport and potential exposure to marine organisms through the estuary, by first evaluating the observed data, then the model data, and finally by investigating the distribution of the age of the model particles; and iii) to investigate how irregular reversed flow events can affect the Al transport and potential exposure to marine organisms.

2. Materials and methods

A coupled numerical model system has been applied to predict the marine transport of riverine Al runoff in Songevann and Nævestadfjorden estuaries as well as through the narrow Lagstrømmen channel and further out through Sandnesfjorden. The model system is based on previous work by Simonsen et al. (2019b). It consists of a hydrodynamic model, which computes the time-varying three-dimensional ocean state and circulation fields, and a Lagrangian transport model, which computes the trajectories of a finite number of synthetic particles that estimate the Al behavior in an estuary-fjord system, including Al speciation and dynamic transformations. The models were coupled off-line, i.e., they did not run simultaneously but rather output from the hydrodynamic model served as input to the transport model. Such a model set-up is common practice in coastal and marine drift simulations (Lynch et al., 2014; Christensen et al., 2018).

2.1. Study site

The Sandnesfjorden fjord system consists of two estuary basins (Nævestadfjorden and Songevann) and Sandnesfjorden, which is connected to Skagerrak in a topographically complicated and shallow sill area with several islands in the fjord mouth (Fig. 1). River Storelva has its outlet located in the inner end of Songevann and is the main freshwater input source to Sandnesfjorden. Storelva is draining Vegårdsvassdraget catchment area (457 km[2]), which is predominantly coniferous forest located in an area that was among the most acidified due to acid rain in southern Norway. Gneiss and granite with limited buffer capacity dominate the rocks in the area, and the effect of acid rain has resulted in acidified water with increased Al concentration due to increased leaching of Al from the catchment. To counteract increased Al toxicity and save fish populations, the
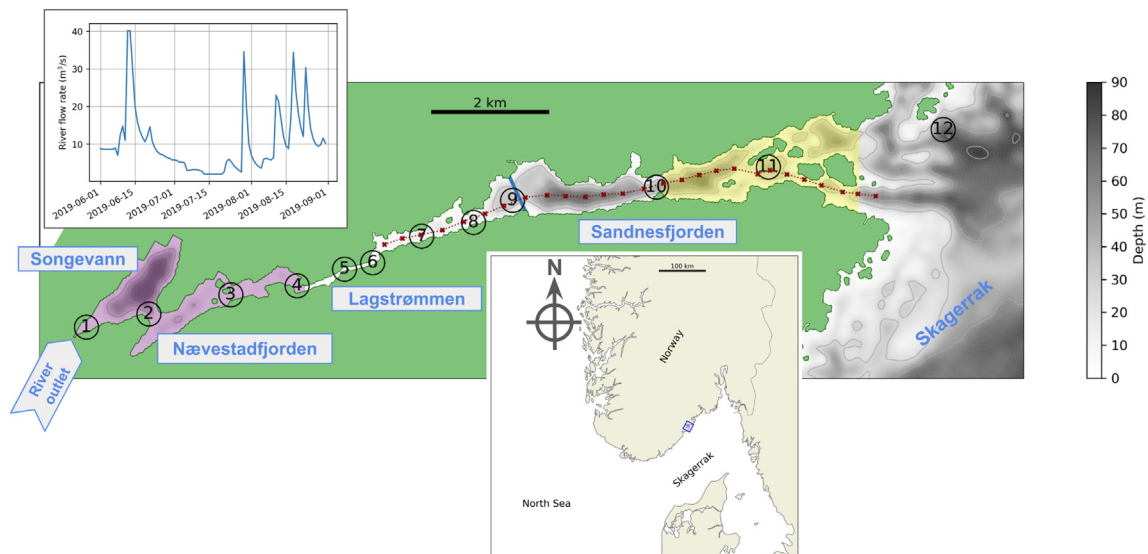
Fig. 1. Map of model coastline and topography in Sandnesfjorden. Depths in the hydrodynamic model are shown by gray shading. Black numbered circles show the locations of the observation stations, from west to east: 1: River outlet (downstream), 2: Estuaries passage, 3: Nævestadfjorden, 4: Doknes, 5: Laget, 6: Pålane, 7: Lagfjorden, 8: Skåttholmen, 9: Hopestranda, 10: Sørlandet feriesenter, 11: Langholmen, 12: Stangholmen. Purple and yellow color shading highlights the two regions for mean age computations. Blue line is the section where the transport is computed. Along-fjord transect is marked with red dotted line. Upper overlay shows the river flow rate from the HBV model for the simulation period. Lower overlay shows the model domain of the high-resolution model (blue square) in an overview map.

watercourse has been limed since 1985 (Direktoratet for naturforvaltning, 2001). There is a seasonal signal in the Al concentration in the river water, with the highest levels in early spring, and the lowest values in early fall, as explained in Appendix A. The average flow rate in Storelva is 13.2 m^3 s^{-1} (Direktoratet for naturforvaltning, 2001), with a typical annual cycle of flooding in spring and fall. The mean flood is 123 m^3 s^{-1} (www.sildre.nve.no). The estuary basins have depths of up to 65 m and are connected to Sandnesfjorden by a narrow channel (Lagstrømmen, around 20 m wide). Sandnesfjorden has a basin of 50–60 m depth located between a shallow inner part and the fjord mouth. Since Sandnesfjorden is a relatively narrow fjord, being about 15 km long and only a few hundred meters wide, the fjord dimensions will greatly reduce the influence of the rotational dynamics caused by the Coriolis force, while the shallow and narrow mouth area will restrict water exchange between the fjord and the coastal ocean. The circulation in Sandnesfjorden is typical for a fjord with river input. The outflow of fresh river water is located in the upper surface layer, and is balanced by an inflow of more saline coastal water in an intermediate layer. Weak currents occur in layers deeper than the sill (e.g. Sætre, 2007). Due to the input of both fresh river water as well as more saline coastal water, the flow is often strongly stratified with distinct vertical gradients, with salinity levels ranging from a few psu in the surface water near the river outlet to 25–30 psu in the deeper layers. The fjord dynamics are mainly driven by large scale density gradients, river freshwater input, wind stress and tides, constrained by the bottom topography (Sætre, 2007). The tides have a maximum amplitude of <1 m (www.sehavniva.no). At Torungen Lighthouse, located around 40 km south of Sandnesfjorden at the Skagerrak coast, northeasterly winds dominate during winter, while southeasterly wind is most common during summer (Sætre, 2007). In Skagerrak, the coastal current has a seasonal signal, with lowest salinity in May–June, coinciding with the maximum freshwater discharge (Sætre, 2007). Therefore, the current pattern is not stationary, but may be characterized by spatial and temporal oscillations at time scales ranging from seconds to decades, and by atypical events which occasionally can reverse the usual pattern of the fjord circulation. We here define 'reversed flow events' as irregular occasions where the surface flow is directed into the fjord over substantial time, triggered by the above-mentioned forces.

2.2. Hydrodynamic model

We have applied the free-surface, terrain-following, primitive equations ocean model ROMS (Regional Ocean Modeling System, http://myroms.org; Shchepetkin and McWilliams (2005); Haidvogel et al. (2008)) to reproduce the fjord dynamics with 32 m × 32 m resolution for the summer period 2019. The highest-resolution model was based on a four-fold nested model system where the horizontal grid was refined from 4 km (the operational forecast model for the Nordic Seas provided by the Norwegian Meteorological Institute and accessible at http://thredds.met.no) to 800 m (presented in detail and validated by Asplin et al. (2020)) and 160 m, all model systems using ROMS. A similar approach for a different fjord area in Norway is explained in detail and validated by Dalsøren et al. (2020). We applied 35 vertical levels with enhanced resolution in the upper 20 m, and this configuration introduced, for instance, 16 vertical levels in the upper 10 m in the grid points where the total depth is 50 m. The model set up is similar to what was explained and validated by Simonsen et al. (2019b), with some improvements. The estuaries Songevann and Nævestadfjorden inside Lagstrømmen were not included in the 160 m model, nor in the experiments described by Simonsen et al. (2019b). To allow a better representation of the dynamics further upstream than in previous studies, we added these estuaries in the highest resolution model. The bathymetry was prepared based on a series of depth measurements from CTD casts close to the sea floor, and a subsequent interpolation of the depths to the model grid. High-resolution coastline data from the Norwegian Hydrographic Service were used to define the land-ocean boundary, and the 32 m-model was set up with a minimum depth of 2 m. Since our focus is on the transport and circulation of surface and intermediate water masses in the entire fjord system with special focus on the marine part (Sandnesfjorden), we considered a horizontal resolution of 32 m × 32 m as sufficient to reproduce the main characteristics of these water flows. Also, we chose a regular instead of an unstructured model grid to prevent a degradation of the resolution in the center of Sandnesfjorden.

The 32 m model was initialized from 160 m model results from January 1, 2019. The 160 m model was run without the estuaries Songevann and Nævestadfjorden, and an iterative extrapolation algorithm was used to provide an initial state for the 32 m model. To compensate for this artificial

hydrography and currents, we defined the first half year as the spin-up period for the model. Tides were applied at the boundaries of the 800 m model and interpolated from the global TPXO7.2 (Egbert and Erofeeva, 2002). The 800 m, 160 m and 32 m models applied high-resolution atmospheric forcing from the non-hydrostatic 2.5 km AROME MetCoOp regional atmospheric model (Müller et al., 2017), provided by the Norwegian Meteorological Institute and accessible at http://thredds.met.no. The freshwater runoff for all rivers applied in the ROMS models were based on daily measurements from the Norwegian Water Resources and Energy Directorate.

Compared with the model setup in Simonsen et al. (2019b), a significant change we performed besides extensions of spin-up period and the model area was to adjust the Generic Length Scale (GLS) turbulent closure parameters (Umlauf and Burchard, 2003). The model simulations in Simonsen et al. (2019b) applied a parameterization equal to Mellor-Yamada 2.5, while our new simulation was set up with parameters more similar to K-epsilon, using the nomenclature of Umlauf and Burchard (2003). Note also that we applied a quadratic bottom stress formulation, while the kinematic surface stress for momentum is parameterized from 10 m winds (see Fairall et al. (1996)).

To analyse the current and hydrographic fields, we have extracted results from the ROMS simulation as 27 vertical profiles in a section along the fjord, starting where the Lagstrømmen channel enters the fjord at Laget and ending just outside the mouth (Fig. 1).

2.3. Transport model

Utilizing currents from the hydrodynamic model, the marine transport of Al was simulated with OpenDrift, an open-source Python-based framework for Lagrangian particle modeling. A detailed description of the transport model functionality can be found in Dagestad et al. (2018). The trajectories of a finite number of numerical particles were computed from a defined release scenario based on the time-varying river runoff of River Storelva (Fig. 1) where each numerical particle represented a certain mass of Al. To estimate the Al behavior in estuaries and fjords, a new module for radionuclides and trace elements was implemented in OpenDrift with functionality similar to the radionuclide module in the TRACMASS model, with functionality and parameters as described by Simonsen et al. (2019a). This module computes speciation and transformation processes with dynamic transformations based on stochastic phase shift algorithms as described by Periáñez and Elliott (2002). A detailed description of the implementation of the radionuclide module in OpenDrift is enclosed in the Supplementary material. This radionuclide module is also applicable for non-radioactive elements (such as reactive metals), and for the present case study, it was configured for Al species adapted from the TRACMASS model, as described by Simonsen et al. (2019b). In the model, each of the numerical units was assigned one of the six model compartments representing the most relevant physico-chemical forms of Al species: LMM anion, LMM cation, humic colloids, polymer, particles suspended in the water column and sediment species. Dynamic transformations between these species were computed at each model time step and were parameterized as relevant transformation processes (sorption, desorption, aggregation, polymerization, remobilization, sedimentation and resuspension), with salinity dependence as described by Simonsen et al. (2019b).

2.4. Observations used for model validation

During field work on August 28, 2019, vertical profiles of salinity and temperature were taken by 56 CTD casts (SonTek's CastAway) at a number of locations from the river outlet throughout the estuary basins and Sandnesfjorden to the open Skagerrak waters. To obtain information about the concentration and speciation of Al in the dynamic water system from river output through Sandnesfjorden, with increasing salinity and limited changes in hydrodynamic parameters during the sampling, it was decided to collect all samples from surface water at 0–0.5 m depth from 12 locations (Fig. 1), with increasing distance from the outlet during one day with minimal time differences. One sample was taken at each location.

Water samples were fractionated *in situ* using membrane filtration (0.45 μm) and ultrafiltration (10 kDa) to avoid changes in Al speciation by storage of samples prior to fractionation. Unfiltered and filtered water samples in triplicate were acidified (5 % HNO_3) prior to determination of Al using ICP-MS (Agilent 8800 ICP Triple Quad). Analyzed certified reference materials (CRM) indicated good accuracy (1640a: 54.0 ± 0.8 μg kg^{-1} compared to CRM value 52.6 ± 1.8 μg kg^{-1}). Measured Al concentrations in ultrafiltered samples were used to identify the concentration of Al in LMM fractions and to obtain information of colloidal and particulate Al species by calculations (Teien et al., 2006).

2.5. Simulation setup

In the transport model simulation period from June 1 to August 31, 80,000 Lagrangian particles were seeded randomly within a volume of 25 m radius and 1 m depth around the location of the outlet of River Storelva (Fig. 1). Seeding of Al was distributed over LMM cation, humic colloid and particle species. Appendix A describes how the releases were distributed in time at 1 h intervals through the whole simulation period as a function of the river water flow rate. No other sources of Al than Storelva were considered. Trajectories crossing the open boundaries of the model domain were permanently deactivated. Hydrodynamic current fields at hourly intervals were utilized to estimate the individual trajectory of each numerical particle at time steps of 30 s. Unresolved sub-grid scale processes were accounted for in the transport model with additional perturbation of the particle positions (diffusion), using a uniform horizontal diffusion coefficient (A_h = 0.25 m^{2}s^{-1}) while the additional vertical diffusion was set to zero. These values were chosen after performing sensitivity tests (not provided here). After the simulation, the model area was partitioned as a grid of equal-sized grid cells (at 40 m × 40 m horizontally). Concentration fields of Al species were then computed at hourly intervals from the number of Lagrangian particles being present within the volume of each grid cell. The concentration fields were smoothed horizontally in space (mean of a square extending 4 grid cells in each direction). Estimates of Al concentration in the surface water were computed as the mean between the surface and a constant depth level.

3. Results and discussion

3.1. Evaluation of the hydrodynamic model

3.1.1. Comparison with hydrographic profiles

Salinity profiles from the 32 m ROMS simulation were evaluated against 56 CTD measurements distributed through the entire fjord as shown in Fig. S1.1. The mean error in the profile was well below 5 psu in the strongly fluctuating surface layer, and there was almost no bias below ~20 m depth. This is a considerable improvement from the results attained in the same fjord in the 2008 experiment described by Simonsen et al. (2019b), in which there were differences of up to 7 psu in the surface layer. Our improvement can mainly be attributed to the extended spinup period, while the change of turbulent closure parameters enhances the model's ability to retain the relatively stable pycnocline in the estuaries upstream of Lagstrømmen.

3.1.2. Average flow

As diagnosed in Fig. 2, time-averaged along-fjord sections of salinity and currents from the hydrodynamic model show a pattern typical for fjords with a thin brackish layer on top of gradually denser water. With the salinity being approximately proportional to water density, the halocline/pycnocline was located at around 1 m depth and the surface salinity/density increased towards the fjord mouth (Fig. 2a). We also found that the model results at Hopestranda compared qualitatively well with the observed salinity profile from the upper ~6 m taken on August 28, 2019 (Fig. 2c), albeit with a small positive bias. The along-fjord current, in this case the east-west current component, had a distinct vertical distribution with flow out of the fjord in the upper ~2 m, weaker flow into
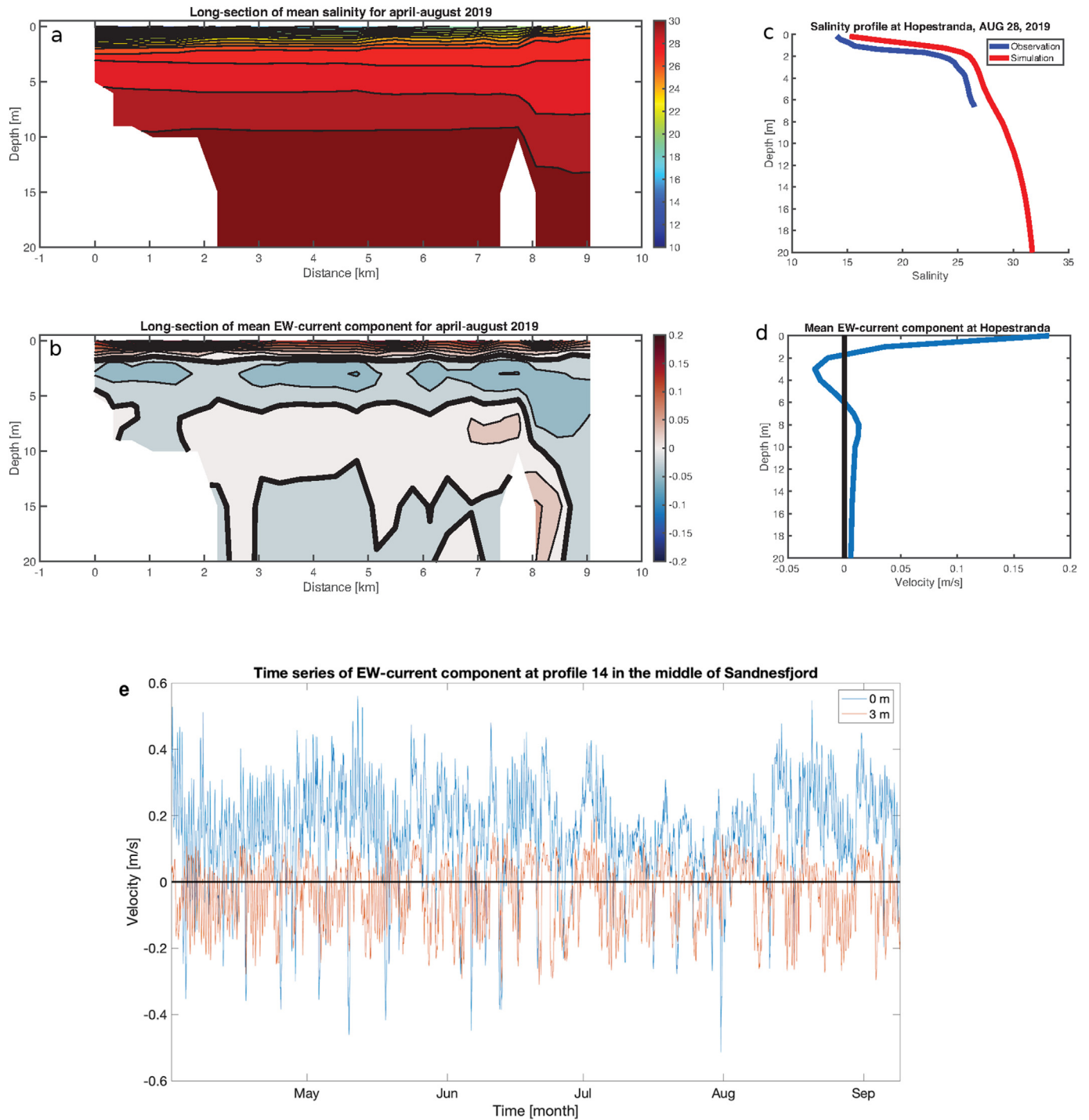
Fig. 2. a) Modeled mean salinity along the fjord for April–August 2019, in the upper 20 m. b) Modeled mean along-fjord current velocity (east/west component) for April–August 2019, with positive values corresponding to flow out of the fjord. c) Modeled and observed salinity profile at Hopestranda on August 28, 2019. Note that the observed profile only covers the upper 6 m and not the whole water column. d) Mean modeled vertical profile of the along-fjord (east/west) current component at Hopestranda. e) Time series of modeled along-fjord (east/west) current component at Sørlandet Feriesenter for surface (blue line) and at 3 m depth (orange line).

the fjord from ~2 m down to ~6 m and under that an even weaker flow out of the fjord (Fig. 2b).

The current structure in the vertical dimension can be characterized from a profile of the mean east-west component of the current at Hopestranda (Fig. 2d). Velocity speeds were on average 0.1–0.2 ms^{-1} in the upper brackish layer and up to 0.05 ms^{-1} flowing into the fjord in the layer between 2 m and 6 m depth.

This vertical flow distribution in the fjord, which in this case reproduced a classical fjord circulation, will be of importance for the transport of contaminants and trace elements by the water currents. Tracers residing in the brackish layer, i.e., in the upper 1 m–2 m, will on average typically be transported out of Sandnesfjorden. Conversely, tracers residing in the layer between 2 m and 6 m depth, will be transported further into the fjord. The sill depth in the mouth area is between 20 m and 30 m, which
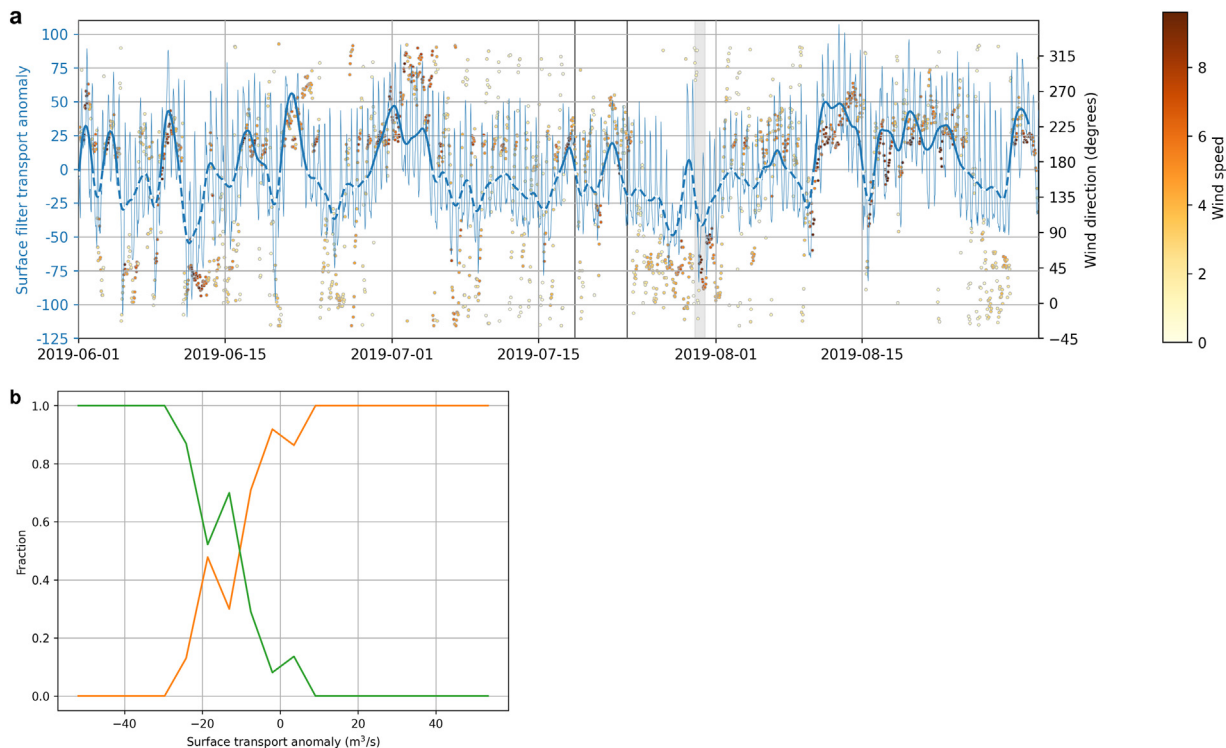
Fig. 3. a) Hourly surface (upper 0.5 m) transport anomaly (thin blue line), temporally smoothed (24 h low-pass filter) transport anomaly of surface water through a cross section at Hopestranda (thick blue line). Negative values are highlighted by dashed line. Circles show observed wind direction (right hand y-axis) and wind speed (indicated by color) at Lyngør lighthouse. The wind directions between 330° and 360° are converted to negative values to better visualize their connection to northerly winds. The two black vertical lines mark July 18 12UTC and July 23 12UTC, the gray field spans July 30 00-24UTC. b) Probability density function of the relative distribution of surface transport anomalies from hydrodynamic model for times with southwesterly winds (orange line) and northeasterly winds (green line). Positive anomaly means that the water transport out of the fjord is higher than the average value. Only times when observed wind speed at Lyngør Lighthouse was 6 ms^{-1} or higher are included.

limits the horizontal exchange of water masses and trace elements below it. Hence, since the settling of particle-bound Al affects the vertical distribution, the affinity of Al to suspended particles and the properties of the available particles being present in the sea water will be of great importance for the transport behavior and spatio-temporal distribution of such trace elements. This comparison with measurements indicates that the hydrodynamic model has reproduced the expected fjord circulation correctly, as it agrees well with the observed CTD profiles (Fig. S1.1). Comparison with the observed salinity profile at Hopestranda (Fig. 2c) shows that the depth of the mixed layer is well reproduced by the model. This implies that the currents in the surface and intermediate layers are reliable, and thus that the mixing processes are correctly described. This is important for the transport fluxes, being essential for the reliability of the Al transport predictions. It also justifies that other phenomena shown by the model are well grounded.

The temporal variability of the modeled east-west current component was relatively large in the upper layers. In particular, a strong tidal signal can be seen at the surface and at 3 m depth (Fig. 2e). The amplitude of the predominantly semi-diurnal tide was up to ~0.1 ms^{-1}. A number of events with flow into the fjord (negative values) at the surface occurred, with relatively strong velocities up to 0.5 ms^{-1}, but these tended to be of short duration. The mean flow structure was relatively stable except for the tidal oscillations and a number of reversed flow events (Fig. 2e). The semi-diurnal tide will typically move the full depth water masses back and forth in one direction for 6 h or approximately 1–2 km.

3.1.3. Reversed flow events

As described in the previous subsection, the surface transport flow is highly variable, mostly due to tides flushing water periodically in and out of the fjord, but also more randomly due to wind forcing and river runoff. As is usual in fjords where an estuarine circulation dominates, the low-

pass filtered flow is mainly directed out of the fjord near the surface, with a compensation flow of coastal water into the fjord in the deeper layers (Section 3.1.2). In the period between June 1 and August 31, the mean surface flow (upper 0.5 m) through a cross section near Hopestranda was 36 m^3 s^{-1}. This is comparable to the input of freshwater from River Storelva (the mean river flow rate was 10 m^3 s^{-1}, see Appendix A) and corresponds well with estuary theory, i.e., that the surface transport is expected to be higher than river input due to entrainment of water from deeper levels (Stigebrandt, 2012). However, as described in Section 3.1.2, the flow can occasionally be significantly different from the prevailing pattern, i.e., outflowing surface water, with weaker or even reversed surface transport. To better visualize the deviations from normal conditions, Fig. 3a shows the surface transport anomaly, i.e., where the mean transport is subtracted; the anomaly is smoothed in time using a 24 h low-pass filter.

The main driver of the surface currents is the wind, where direction, strength and duration time are important factors. From Fig. 3a one can spot that the events with strong negative anomalies in the surface transport all appeared under conditions with easterly and northeasterly winds[1] (−30° to 150°), while the high transport anomalies occur during westerly and southwesterly wind directions (150°–330°). In calm conditions, the correlation was low, but at stronger winds (above ~6 ms^{-1}), there was a clear signal of strong positive anomaly at SW wind direction, and strong negative anomaly at NE direction. However, an exact correlation was not expected, as winds may shift more rapidly than the time it takes to change the flow pattern in the fjord. This is further emphasized in Fig. 3b, which shows the distribution of surface transport anomalies for the two wind direction regimes (northeasterly and southwesterly) for occasions with wind speed

---

[1] We use a meteorological convention where the reported wind directions denote where the wind blows from. The wind directions between 330° and 360° are converted to negative values to better visualize their connection to northerly winds.

above 6 ms^{-1}. Here, there was a clear dominance of negative transport anomaly situations under northeasterly wind directions. Situations with transport anomalies around the mean values occurred at both wind directions, while the strong positive transport situations occurred when the wind was southwesterly.

Within the studied time period the most typical occasions of reversed flow forced by strong northeasterly winds were at May 4, May 8, May 17, June 10, July 30, August 11 and August 15 (Fig. 3a). The episode on July 30 will be discussed in detail in Section 3.3.

3.2. Assessment of aluminium transport estimates

3.2.1. Observational data

Observed Al concentrations and salinities are reported in Table S1.1 and plotted in Fig. 4a. Since Storelva is the main source of Al to Sandnesfjorden, mixing of the river water with saline coastal water gave a close to linear decreasing trend of observed Al concentration with increasing salinity. However, at the estuary stations (River outlet, Estuaries passage, Nævestadfjorden and Doknes), there were only small differences in total Al concentration (156 µg L^{-1} to 165 µg L^{-1}) and in salinity (2.3 psu to 2.8 psu), which indicates homogeneous surface water and that mixing with coastal water played a minor role at the time of sampling in that part of the fjord.

Outside of Laget the Al concentration increased, suggesting different water masses to be present outside the narrow Lagstrømmen canal. From the Laget to Pålane stations, the total Al concentration increased from 147 µg L^{-1} to 168 µg L^{-1}, while the salinity increased from 4.6 psu to 5.2 psu. Further out, through the stations in Sandnesfjorden (from Pålane to Stangholmen stations) the relation between Al concentration and salinity was again close to linear, but the slopes appear to be somewhat different on either side of Lagstrømmen. Non-negligible, additional sources may be an explanation, but it is more likely to be a result of changing Al concentration in the runoff in River Storelva, since high river flow events can give increased Al concentrations (Teien et al., 2006). This is supported by the fact that there was a high river flow event in Storelva about 7 days before the time of sampling (Fig. 1), which corresponds with the computed age of the surface water in Sandnesfjorden (Section 3.2.3).

At Stangholmen station, located outside the fjord mouth where the water can be assumed to be representative for the coastal current, the salinity was 25.3 psu, and the total Al concentration was low (7.7 µg L^{-1}).

Although the measurement error is low (typically a few percent), errors due to interpolation and representativity of the timing and location of the sample may also be considerable (Kanamitsu and DeHaan, 2011; Sandvik et al., 2016). This should be kept in mind when interpreting the model-observation comparison.

3.2.2. Model estimates of total Al concentration

The spatial distributions of modeled total Al concentration levels (sum of all species) at the surface, intermediate and deeper layers, averaged over a time interval covering the field sampling time, are shown in Fig. 4 b, c and d, respectively. On this day, the modeled surface Al concentration was relatively low in and near the narrow Lagstrømmen channel, with higher values in the estuaries and in Sandnesfjorden. The surface concentration levels (Fig. 4b) decreased along the fjord transect from the river outlet towards the Lagstrømmen, after which they again rose and decayed towards the fjord opening, which agrees well with the observed pattern. However, the modeled spatial distribution was highly variable, with large horizontal gradients and accumulation of Al in patches of high concentration near the shore. At intermediate depths (2 m–7 m), one patch with high values was present in the central Sandnesfjorden near Hopestranda (Fig. 4c), while in the deeper layers the concentration was very low, more than two orders of magnitude lower than at the surface (Fig. 4d). These low concentration levels in the deeper water indicate that most of the transport, at least on the time scales involved in our simulations, occurs near the surface. It would probably take years beyond our simulated time period for the model to achieve a realistic distribution of the Al stored and transported

by sediments and suspended particles near the bottom. Therefore, we should be aware that our model simulations may underestimate the concentrations somewhat in the deeper water where sediment interactions are significant. However, this is assumed to a play minor role for the evaluation of the surface Al concentrations that is performed here. The patches seen in the surface field are not stationary, but follow the prevailing water transport out of the fjord towards the open ocean. Hence, with model results indicating changes of more than a factor of 10 over short distances, the location and timing of the sampling will have large impact on the measurements and subsequently on the model validation. In this case, the modeled surface Al concentration field was more scattered than what was indicated by the surface observations, which suggests a more gradual decrease with distance from the Lagstrømmen channel.

Model time series of surface (mean between surface and 0.5 m) total Al concentration from an 11-day period around the sampling campaign from four selected sampling sites are plotted in Fig. 5 (a–d). The model results on August 28 are compared with the observations at all sampling sites in Fig. 5 (e, f). (Comprehensive results are available in Table S1.1 and Table S1.2). In general, at the estuary sites in Songevann and Nævestadfjorden (Estuaries passage, Nævestadfjorden, Doknes), as well as through the narrow Lagstrømmen (Laget, Pålane) and in the inner part of Sandnesfjorden (Lagfjorden, Skåttholmen), the model underestimated observed Al concentrations, while the model slightly overestimated near the river outlet and at the sites in the outer part of Sandnesfjorden (Hopestranda, Sørlandet feriesenter, Langholmen). Except for the stations within the Lagstrømmen channel, where the model underestimated by a factor of 4–5, and at Langholmen where the model overestimated by a factor of 3, all model values deviated from the observations by less than a factor two, which can be considered as good agreement for model estimates of tracer and contaminant transport. Overall, our results have a mean error of −26.8 µgL^{-1}, and a mean ratio of 2.4 (Table S1.2). Although the underestimation through Lagstrømmen seems considerable, one should remember that this is a shallow and narrow region, covering a relatively small part of the total domain. The focus in our study is the marine part of Sandnesfjorden (outside Laget) where the model skill in fact is very good. However, as seen from both the spatial distribution and the time series, the spatiotemporal variations of the modeled concentration estimates were large, and the timing of the high concentration patches may have played an important role for the validation results. As demonstrated by Elskens et al. (2014), the variability in time and space is considerable also for the observational data in estuaries, and biases up to one order of magnitude can be expected.

The variability changes with time, as indicated by the dotted lines in Fig. 5 (a–d), which shows the standard deviation within each ± 24 h interval. Obviously, this changes with both time and location, reflecting that some periods have low variability while other periods have larger temporal variations. In general, the variability was high, with magnitudes of the standard deviation being sometimes as high as the value of the Al concentration itself. The overall root-mean-square error of 80 µgL^{-1} (Table S1.2) is of the same magnitude as the model standard deviation at the Hopestranda and Sørlandet Feriesenter stations, indicating that the observed values lie within the range of the model estimates. The systematic underestimation in the estuaries and overestimation in the outer fjord may suggest a too strong flushing of Al-contaminated water out of the fjord in the model. But it could also partially be due to artificial effects from the configuration of the post-processing software when the transport model data are converted from individual particle positions to continuous concentration fields. As explained earlier, the Al concentrations are extracted by summing the numerical units within a certain volume at hourly intervals, and later smoothing the values both in time and space. Hence, the dimensions of the volumes over which we integrate, and implicitly assume homogeneous distribution, affect the results, as concentration levels computed over smaller grid cells provide more details but also involve more noise as each individual trajectory going in or out of the volume will have a larger impact. The specific choice of parameters might give good representation of the natural conditions in one part of the domain, while the
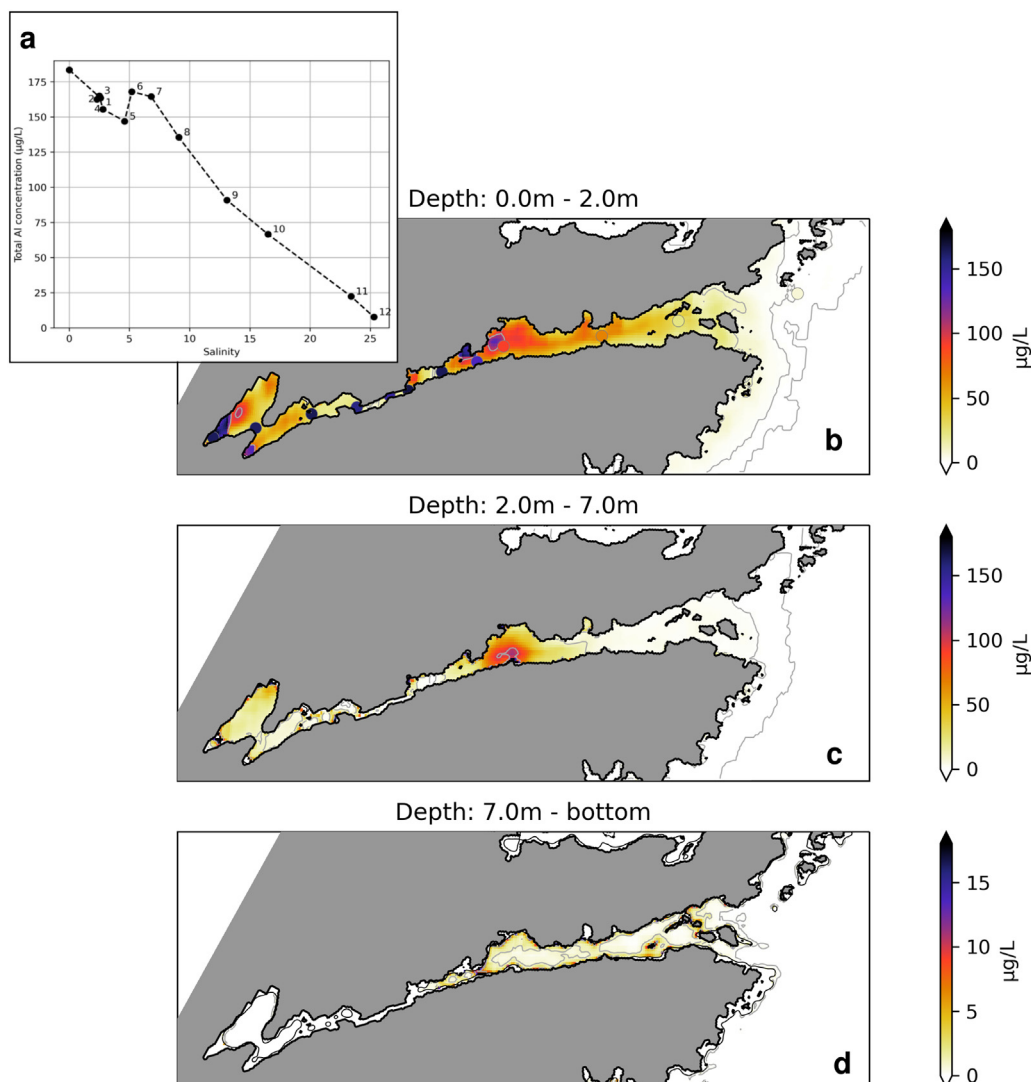
Fig. 4. a) Observed total surface Al concentration from Storelva, the estuarine basins and Sandnesfjorden. Numbers refer to the location numbering in Fig. 1 and Table S1.1. The upper left point without number is from the sample taken in the river. b-d) Spatial distribution of modeled Al concentration in b) surface (0 m–2 m), c) intermediate (2 m– 7 m) and d) deeper water layers (below 7 m) averaged over 06:00UTC to 12:00UTC on August 28. Note different color scale for the deeper layer. Observed surface Al concentrations are shown by colored circles in panel b. Contour lines for 0.1, 1, 10 and 100 $\mu g\ L^{-1}$ are drawn with gray. Thin solid line in bottom panel shows the 7 m depth isoline.

representativity might be less good in other areas. This is particularly the case for the choice of depth for the vertical integration (Δz) for which the gradients may be considerable. The value of Δz should ideally be the depth of the surface mixed layer and hence vary along the fjord transect. In the presence of strong vertical gradients, integrating too deep below the surface layer implies that a larger fraction of deeper water with lower concentration levels is included, and hence the model output will be underestimated. Conversely, choosing a too small Δz would give rise to artificial noise, due to the discrete nature of the trajectory model. Although a full sensitivity analysis has not been conducted here, some tests indicated that such choices of model parameters in the setup and post processing may affect the model results with a factor 2–3, which is comparable to the model errors. The degree of horizontal smoothing will also be a matter of concern, as stronger smoothing may compensate for artificial noise such as false stranding at the coastlines, but will also conceal real variability in the concentration fields.

Although our simulations with the hydrodynamic model have high resolution (32 m × 32 m in the horizontal) compared to present state-of-the art operational models, e.g., NorKyst800 at 800 m × 800 m (Albretsen et al., 2011), there are still sub-grid scale dynamics that are not resolved

properly. The physical dimensions of Sandnesfjorden, including the estuaries and Lagstrømmen, are small, <20 m across at the narrowest place. Even though the hydrography was well reproduced by the model, using input data at 1 h temporal resolution for the transport estimates might give unexpected artificial impacts such as false stranding and unrealistic paths through the complex topography. To compensate for the unresolved dynamics, an additional horizontal random-walk diffusion was added to the trajectories. However, the current parameterization of diffusion in OpenDrift is relatively primitive, inasmuch as it is set to a uniform value, without taking the dynamic flow properties into account. Therefore, since the model resolution is relatively high, a relatively low value was chosen, not for the purpose of correctly reproducing the turbulent flow properties, but instead to secure some smoothing of the numerical particles with small random displacements. In the vertical dimension, the advective flow appeared to give sufficient spread, and adding more diffusion would result in weaker gradients. Our rough estimate was based on experience from a series of sensitivity tests.

The modeled settling and sedimentation is primarily determined by the particle size distribution, which is a relatively simple approximation (normal distribution around a mean value with a given standard deviation),
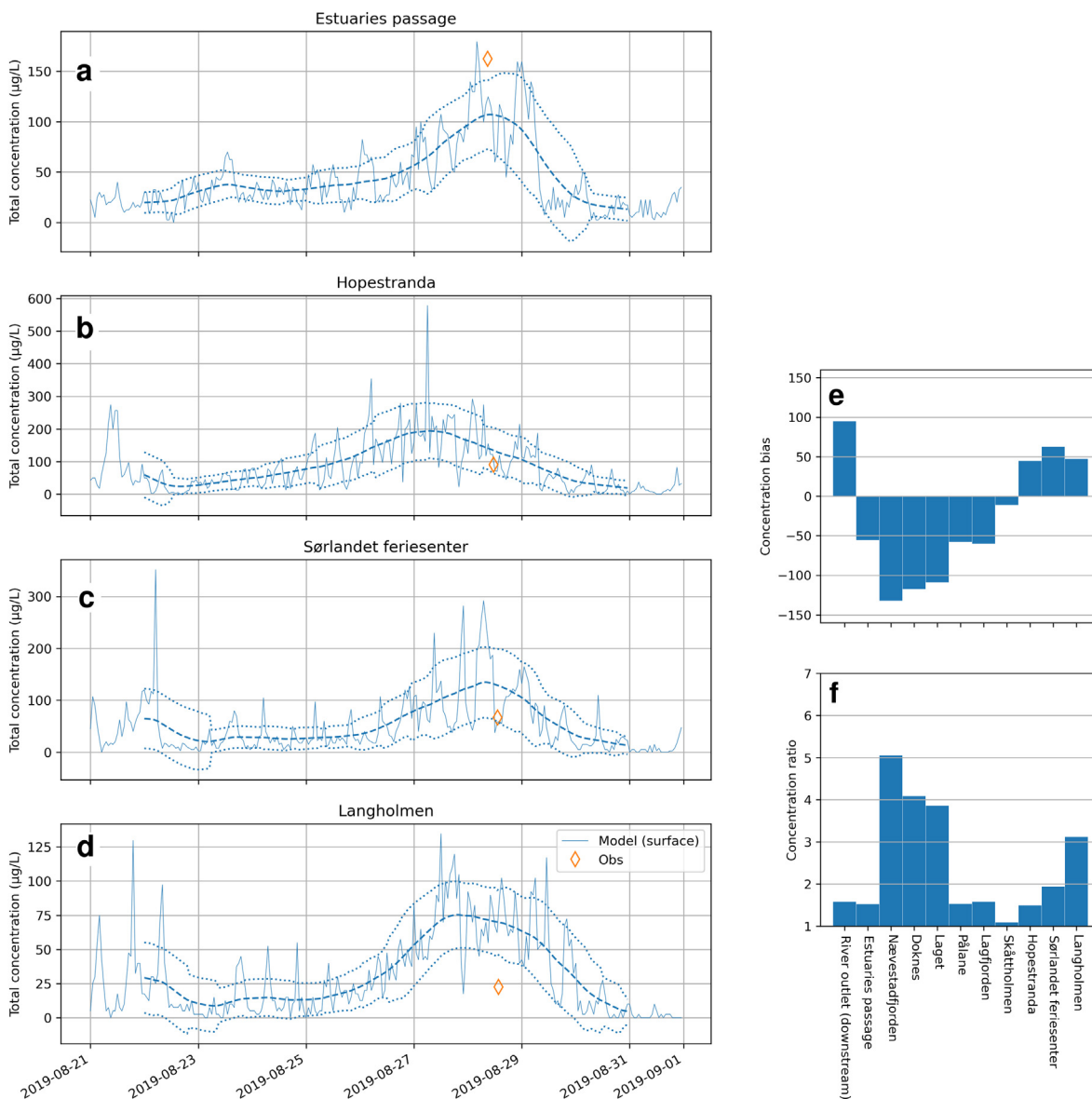
Fig. 5. a-d) Model estimated of surface Al concentration (mean of 0 m to 0.5 m depth) in four of the sampling locations. Thin solid line is hourly estimates, thick dashed line is weighted smoothed mean (± 24 h), thin dotted lines are 1 standard deviation of the mean. Note different scales on y-axis. Orange diamonds are observed total Al concentration. e-f): Bias (total model Al concentration (C_m) minus observed total concentration (C_o, e)) and ratio (f) between model and observed total surface (0 m–0.5 m) Al concentration at the sampling sites. Ratios are computed as $\frac{C_m}{C_o}$ when $C_m > C_o$ and $\frac{C_o}{C_m}$ when $C_m < C_o$.

but attempts to cover the most relevant part of the real particle size distribution. As already mentioned, small deviations between the real particle size distribution and the model approximations or parameterizations may be able to influence the vertical distribution of the contaminants and, hence, the model results considerably. In our case, in the natural bottleneck at Lagstrømmen, the vertical mixing is generally increased. This subsequently affects the vertical distribution, settling, sedimentation and resuspension further out through Sandnesfjorden. Other model settings that plausibly may affect the results are assumptions about discharge rates as well as the parameterization of horizontal and vertical sub-grid scale processes. However, we have made our choices of parameters and assumptions attempting to give the best overall representation of the real environment and to be best fitted for comparison with observed Al concentration under the given circumstances.

Although estuarine circulation has been modeled with slightly higher horizontal resolution using unstructured grids (e.g., Zhao et al., 2010), the benefits of increased resolution may be minor in our case. Using unstructured grids also comes with some drawbacks. Firstly, an unstructured

grid does not yield more grid points. The increased resolution in certain areas must be compensated for with coarser resolution in others. In this study, the focus is on transport processes in the fjord, aiming at resolving the variability associated with relatively small eddies. Secondly, the time-step criterion is determined by the smallest grid cell, imposing an unnecessarily small time step for the cells with coarser resolution, and hence a more computationally expensive model with enhanced artificial numerical diffusion in larger parts of the model domain. Considerably higher resolution would also lead to issues regarding the available bathymetry data, and it would challenge the assumption of hydrostatic flow. In the end, the present hourly, 32 m × 32 m resolution in the ROMS output should be sufficient for our purpose, which is to resolve the main dynamic features driving the transport. It might miss some small-scale events related to turbulent and non-linear features, but these are assumed not to affect the general fjord circulation substantially. Calibration and validation performed in already published work (Simonsen et al., 2019b), as well as the validation performed here, show that our model results are reliable, with respect to the available observational data. Therefore, we can assume that the large variability seen

in the modeled surface concentration is plausible. Such model results can provide important additional information to what is shown by the observational data, highlighting areas potentially exposed to the accumulation of contaminants. Similar patterns are likely to be present in other fjords as well, also for other metals and contaminants. However, due to complex dependencies on external forcing (such as river flow, wind characteristics, geochemical conditions), a few issues cannot easily be accounted for and should be subject for further investigations, although estimation of the uncertainties involved is not straight-forward. We consider that the most important issues that should be looked into to include: the contribution of Al from other nearby fjords, the river input of Al speciation and, finally, the parameterization of the species transformations in coastal water. In addition, for a more detailed evaluation of the model, longer time series and wider spatial coverage of measurements are required, in order to assess the spatio-temporal variability in the fjord under a broader range of environmental conditions.

3.2.3. Mean age of modeled Al

Lagrangian models keep track of the pathways of each single trajectory and statistics of the age and transport times can easily be extracted from the model output. Here, the term 'age' refers to the number of days since a Lagrangian particle was released from the Storelva river outlet in the transport model. Since the trajectories may follow a number of different paths to a given location, 'mean age' is the average of all Lagrangian particles present within a volume within a given time interval. To illustrate how dynamic effects in the flow can affect the mean age, we have computed time series of the mean age of the Al contaminants of all species for surface (0 m–1 m) and two intermediate depth layers (1 m–3 m and 3 m–6 m). Time series for July and August are shown for two basins; estuaries and the outer part of Sandnesfjorden (Fig. 6) with extent highlighted by purple and yellow color shading, respectively, in Fig. 1. The surface layer in the estuaries rapidly achieved a quasi-steady state, and kept a mean age at less than five days through the simulation period. Still, after a month simulation time, the

mean age in the outer basin as well as the layers deeper than 1 m in the estuaries increased near monotonically from the beginning of July until it dropped and a quasi-steady state was reached in the latter half of July. In general, such a monotonic increase in age (e.g., as seen in the 3 m–6 m depth interval in the estuaries between July 1 and July 25) indicates low exchange of contaminants, where few trajectories escape the basin and few new enter that depth interval. In contrast, a decreasing trend in the mean age may be caused either by amplification of the input of young particles, or an increased outflow of old particles. Such episodes may be triggered by external forcing like wind and river flow, giving rise to changes in the horizontal or vertical flow or enhanced mixing events. Steady state conditions occur with a close to constant mean age, as seen in the surface layer in the estuaries. In such episodes, the input of new particles is approximately balanced by the outflow of old particles. Large difference between the different depth levels, as seen in the estuaries through the whole period, means that there is strong vertical stratification and little exchange of Al between the different depth layers. In contrast, similar values for different depths, as seen in the outer basins, means that the water masses are well mixed vertically. The model results indicate that the vertical stratification of the water masses and Al concentration became gradually weaker further out through the fjord, not only due to increased mixing of the water masses, but also as an effect of the settling of particle-bound Al species.

As expected, since the transport out of the fjord is fastest near the surface, the age was lower closer to the surface than in deeper water layers at almost all times. Further, due to the general transport direction out of the fjord, the mean age of Al in the surface water was generally increasing with distance from the river outlet and was higher in the outer part of the fjord than in the estuaries. This gave mostly positive values for the age difference in Fig. 6c. However, this was not always the case for the two intermediate water layers, in which we earlier have seen transport directed into the fjord. In the estuaries, the larger depths and stronger stratification will allow the settling particles and other species that sink or mix down into the deeper layers to achieve longer residence times than in the outer basin.

There were a couple of periods of decreasing mean age in both basins, which can be attributed to periods with high river flow rate (Fig. 1), during which water with high Al content was introduced and flushed through the fjord. After a period with low runoff and increasing mean age in July, the increased runoff was again visible as decreasing mean age of the Al contaminants around July 20. Interestingly, the mean age in the surface water in the estuaries stayed steadily low (below five days), while mean age in the deeper layers continued to increase. This indicates that the Al transport in the upper surface layer rapidly became balanced, and Al in the deeper layers was only occasionally flushed down from the surface water. In the period approximately between July 10 and July 30, the difference between the mean age of Al in the surface in the outer fjord and estuaries increased and was at its largest, up to >20 days, in late July (Fig. 6c). This increasing difference indicates that the transport time through Sandnesfjorden increased through this time period, with accumulation of Al contaminants in the inner basins. Later, in August, the mean age difference was relatively steady between 5 and 10 days.

A sudden change is clearly seen in all time series in the last days of July, as a dramatic drop in mean age followed by a relatively low and steady mean age for the rest of the simulation period. This change is a result of a reversed flow event, as described in detail in Section 3.3, with a sudden vertical redistribution of Al. This enhanced vertical mixing also made the horizontal gradients smaller, with low mean age differences between outer fjord and estuaries in all the considered depth intervals (Fig. 6c).

3.3. Tracer transport during reversed flow events

To evaluate how the reversed flow events potentially may impact the distribution of water masses and tracers, we will look closer at the conditions in Sandnesfjorden during July 29 to August 1, one of the most pronounced events with reversed flow. A similar event was discussed by Simonsen et al. (2019b).
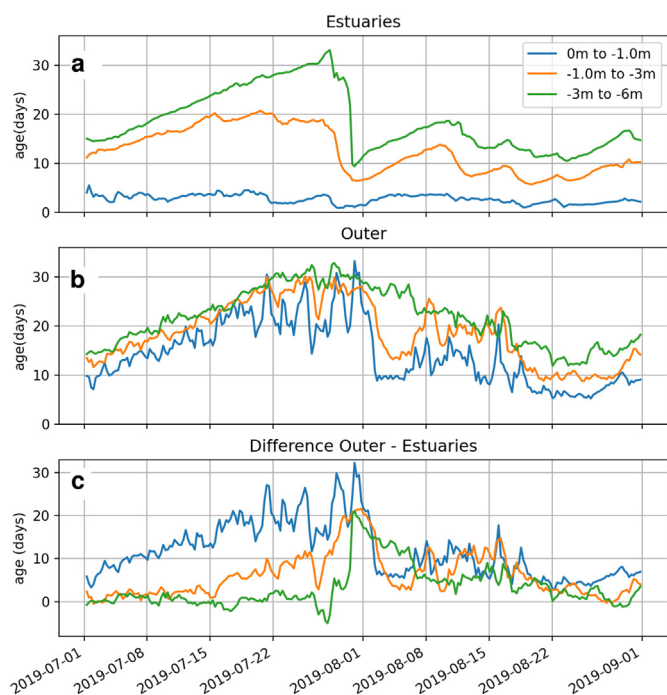

Fig. 6. Time series of mean age in the estuary basins (a), the outer part of the fjord (b) and the difference between these basins (c), divided into depth intervals. The spatial extent of the 'Estuaries' and 'Outer' basins are marked with purple and yellow color shading in Fig. 1, respectively.

July started with a period of relatively strong SW and W winds (200°–300°, 7–10 ms^{-1}) and strong positive transport anomaly, followed by a period of light winds (Fig. 3a). After two short periods of SW winds (July 18, July 23) and positive transport anomaly, the winds were almost exclusively directed from NE and increasing through the rest of July. Therefore, the transport was low with mostly negative anomalies from early July until the event at July 30 (Fig. 3a), i.e., low surface flow and accumulation of fresh water in the inner part of the fjord, as already discussed in Section 3.2.2. During these days, the wind was able to reverse the surface currents in Sandnesfjorden. On July 30 00UTC the typical situation with an outflowing surface brackish layer was present (Fig. 7a), but in the morning of July 30, the winds increased to >10 ms^{-1} from NE, so that 12 h later (12UTC) the wind had forced the surface currents to flow into the fjord all the way to Laget (Fig. 7b), resulting in a rapid reversed surface flow into the fjord.

Due to the wind pushing the upper layer water into the fjord during the event, the river input of fresh water was blocked and accumulated in the inner part, causing a sharp front between fresh and saline surface water to be established (Fig. 7b). Not only the surface water was affected, but a similar pattern also extended down into the deeper layers (not shown in figure). In the evening, decaying winds led to enhanced surface flow out of the fjord. Due to the outbreak of the accumulated fresh water, the vertical stratification became stronger than before the event.

In combination with other processes (such as tidal mixing, particle settling, etc.) these events also affect the Al concentration in the fjord. The time series of modeled Al concentration shows a significant increase at Hopestranda station during the reversed flow event (Fig. 8b), with accumulation of Al due to inflow. Around noon on July 30, there was a sudden decrease due to the flushing and strong outflow of surface water. Similarly, at Estuaries passage station (Fig. 8a), the Al concentration decreased very rapidly during the event. At Hopestranda, a new peak appeared at July 31, while at Sørlandet feriesenter (Fig. 8c), there was a peak around noon at July 30, which may be attributed to flushing of a plume of water with high Al concentration during the reversed flow event. At the outermost station, Langholmen (Fig. 8d), no clear signals of the event are visible.

The mean age of the modeled Al contaminants, an indicator of the residence time of water masses in the fjord, increased through July, with

low flushing and a net increase of Al in the inner part of Sandnesfjorden (Fig. 6a). As already mentioned, the low river flow throughout July resulted in increased mean age, particularly in the deeper layers. The reversed flow event in late July increased the vertical mixing in both the estuaries and the outer basins and yielded reduced vertical stratification, increased mean age at surface and reduced mean age in the deeper layers. Later, stronger stratification was re-established in the estuaries from July 31 lasting through the first half of August. The mean age again increased in the deeper layers, and remained relatively low at the surface (Fig. 6a). From these considerable changes in age and distribution of Al concentration, it is clear that the effects of such short-term reverse flow events can have consequences for the hydrography for long time periods. This illustrates the need to take short-term variability into concern when evaluating the potential environmental impacts, such as assessment of the spatio-temporal distribution of potentially toxic Al species.

The continual mixing of freshwater and seawater in coastal waters makes estuaries and fjords highly dynamic, as illustrated in this work. When contaminants are transported with the freshwater rivers, accurate models are needed to predict changes in coastal water quality during different hydrodynamic conditions, as it is very challenging to obtain similar information by sampling only. Models can also be used to identify locations that need more attention, e.g., to select where and when to sample, or to identify locations with minimum risk of contaminants in recommendations of where to locate installations such as mussel farms or fish farms.

4. Conclusion

For estimation of the environmental effects of contaminants (e.g., biological exposure), high-resolution models capable of resolving the instantaneous concentration and peak values at high spatial resolution throughout estuaries are important to reveal deviations from the average values, since episodic events with reduced water quality can cause adverse effects. In such cases, detailed estimates are necessary for transport predictions of contaminants in fjords and coastal regions. In this study we have combined hydrodynamic and transport model data with observations to investigate the impact of dynamic features on the transport of Al in Sandnesfjorden. The validation of the model data from the underlying
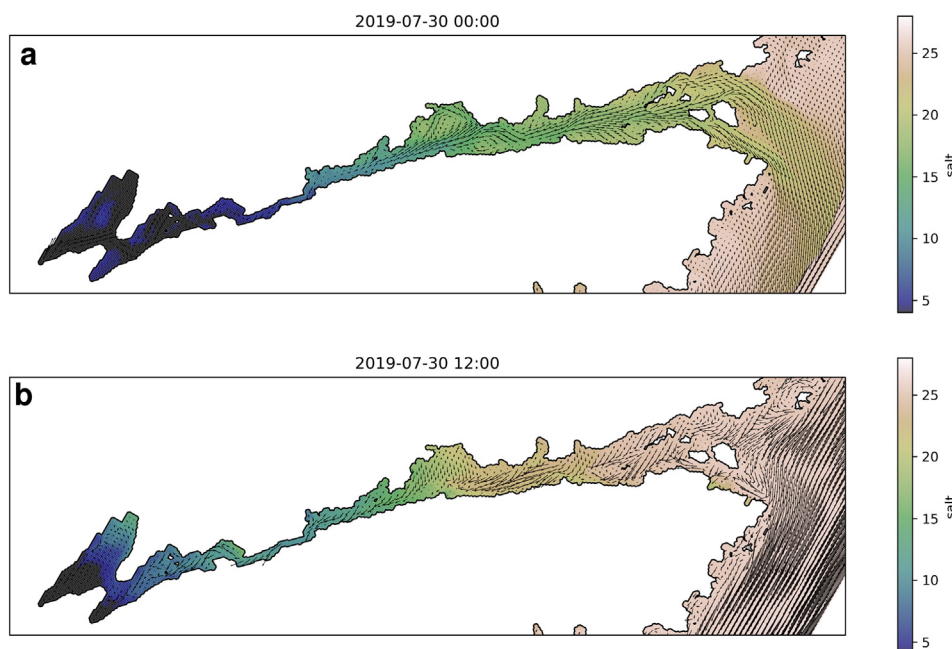

Fig. 7. Current vectors and salinity at the surface for July 30, 00 UTC (a) and July 30, 12 hUTC (b).
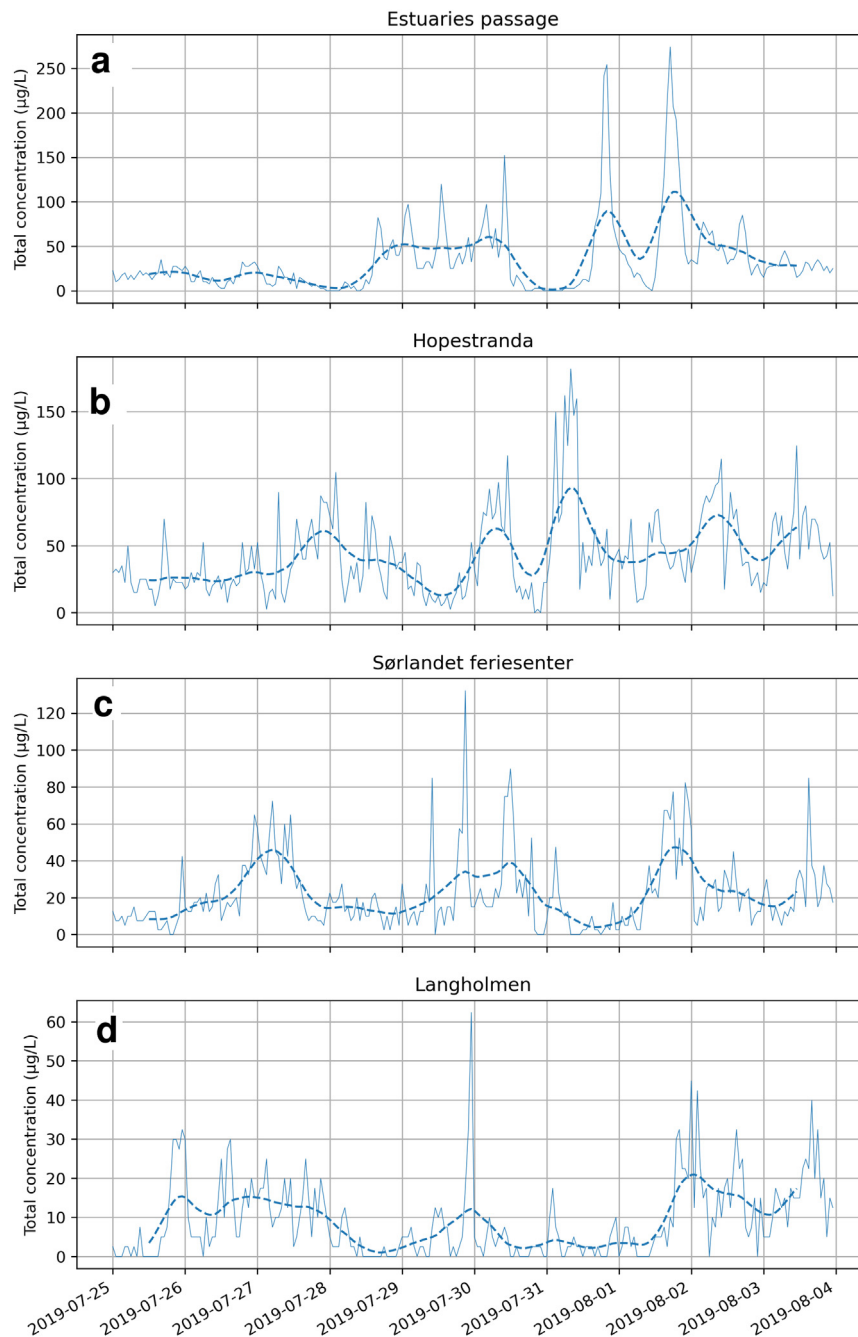
Fig. 8. Time series of surface Al concentration at four of the sampling stations during the reversed flow event in end of July 2019. Thin solid line is hourly estimates, thick dashed line is weighted smoothed mean (±12 h). Note different scales on y-axis.

hydrodynamic model showed improvements compared to previous studies (Simonsen et al., 2019b) due to targeted optimization of the model configuration. The model overestimates the salinity with <4 psu, and has a good agreement with the observed thickness of the surface layer. The transport modeling gave a detailed picture of the Al concentration in Sandnesfjorden and suggested more scattered and variable fields than what was indicated by the observational data. Although the observations apparently showed smoothly decreasing Al concentration in the surface water along the fjord, the model fields suggest stronger horizontal gradients. Therefore, lateral gradients across the fjord as well as hot spot regions indicated by the model should be expected and be further investigated in future sampling campaigns. Although the narrow Lagstrømmen channel turned out to be

challenging for the model, the evaluation showed that the modeled Al concentrations corresponded well with the observed values in most parts of Sandnesfjorden and in the estuaries. Through Sandnesfjorden, the difference between model and observed total Al concentration was less than a factor 2. In total, the new model developments have improved the results compared to previous studies, also for the transport model. The model validation indicates that the results are reliable, and that the features revealed by our model in this particular case (patchy distribution with large variations in time and space) most likely are characteristic of other fjord estuaries.

In addition to the variability of contaminant exposure caused by river input, strong winds into the fjord opening occasionally triggered

reversed flow events with surface transport into the fjord in strong contrast to the average flow. During these events, considerable mixing and redistribution of the different water masses occurred. This affected both the horizontal distribution, with coastal water being pushed into the fjord and blocking the river discharges temporarily in the inner part of the fjord, as well as the vertical distribution when surface water is mixed with deeper water masses. Such events may considerably affect the properties of the water as well as the contaminant concentrations and transport times in fjords. The wind speed and direction was found to be the one of the primary drivers for both the frequency and magnitude of these reversed flow events. At moderate and high winds (above ~ 6 ms^{-1}) the transport anomaly, one of the primary effects of the reversed flow event, was strongly correlated with wind direction.

The new results from this paper should be relevant and important for model development and for interpretation of results from models estimating or predicting transport of any contaminant in fjords and coastal regions. For instance, in environment management, new installations or any other activities or assessments involving contaminants in coastal environments, we therefore underscore the need of performing realistic and reliable model experiments. Especially for the estimation of biological exposure, the instantaneous concentration and peak values are important, which are not usually captured by sampling campaigns. Therefore, our results demonstrate that detailed estimates are necessary to show the variability in time and between locations, in regard to the potential for contaminant exposure (concentration and duration) for marine wildlife as well as for aquaculture and fish farms. In contrast to in-situ measurements where only instantaneous states are captured, our study demonstrates the importance of utilizing a model system where all relevant dynamic and geochemical processes are taken into account.

CRediT authorship contribution statement

Magne Simonsen: Writing – original draft, Methodology, Conceptualization, Investigation, Data curation, Software, Formal analysis. **Jon Albretsen:** Conceptualization, Methodology, Validation, Writing – review & editing. **Øyvind Saetra:** Conceptualization, Writing – review & editing. **Lars Asplin:** Conceptualization, Methodology, Validation, Writing – review & editing. **Ole Christian Lind:** Conceptualization, Methodology, Investigation, Writing – review & editing, Project administration, Funding acquisition. **Hans-Christian Teien:** Conceptualization, Methodology, Validation, Investigation, Project administration.

Data availability

Data will be made available on request.

Declaration of Competing Interest

The authors declare that they have no known competing financial interests or personal relationships that could have appeared to influence the work reported in this paper.

Appendix A. Estimation of Al run-off

The run-off of aluminium (Al) from river Storelva is assumed to be present as low molecular mass (LMM) cation, humic colloid and particle species. The concentrations of each of these species are estimated with an algorithm as described in the following.

First, measurements of total Al concentration taken between 2002 and 2008 in river Storelva at Nes Verk, 11 km upstream of the river outlet (Fig. A.1) (Kroglund et al., 2011) reveals a strong seasonal cycle in the total Al concentration, with highest concentration in late winter/spring and lowest values in late summer/fall. To take this variability into account, a primary (temporary) estimate of the total concentration C'_T is the monthly mean of these measurements for the month of interest (Table A.1, orange stars in Fig. A.1).
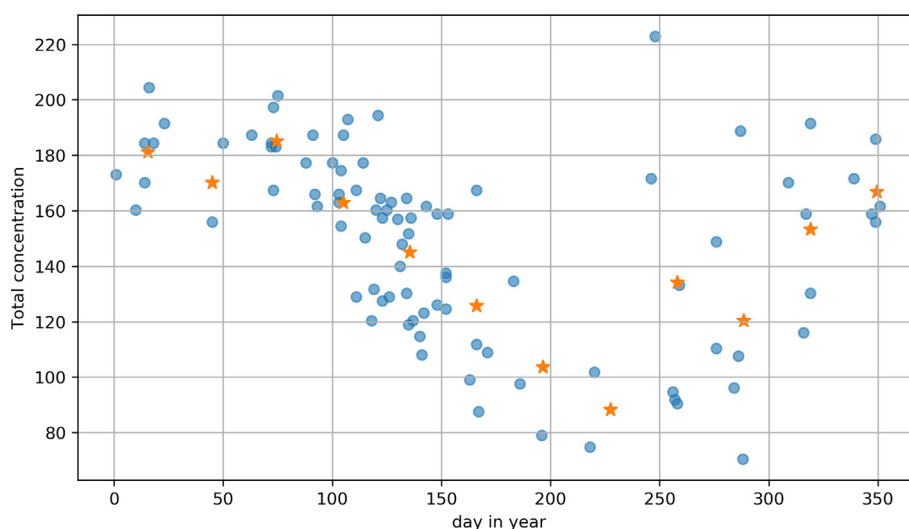

Fig. A.1. Measurements of total Al concentration (blue circles, unit: µg L^{-1}) from Nes Verk between 2002 and 2008 (Kroglund et al., 2011). Orange stars are monthly mean values.

Table A.1

Monthly mean total Al concentration (µgL⁻¹) from Nes Verk.

Jan	Feb	Mar	Apr	May	Jun
181.2	170.2	185.2	162.9	145.1	125.7
Jul	Aug	Sep	Oct	Nov	Dec
103.7	88.3	134.1	120.4	153.4	166.8

The LMM cation and humic colloid concentrations are assumed to be constant fractions of C'_T,

$$C_{LMM} = C'_T \cdot f'_{LMM} \tag{A.1}$$

$$C_{COL} = C'_T \cdot f'_{COL} \tag{A.2}$$

We have used values of $f'_{LMM} = 0.3$ and $f'_{COL} = 0.5$, similar to Simonsen et al. (2019b).

The concentration of particle-bound Al is assumed to vary with the river flow rate F, due to stronger resuspension of bottom sediments during high flow (Crawford, 1991). First, the total suspended sediment concentration (TSS) is estimated, assuming log-linear relationship between F and TSS:

$$\ln (TSS) = A \cdot \ln (F) + B \tag{A.3}$$

Here, the TSS observations are taken close to the outlet of Storelva in 2017 and 2018, extracted from "Miljøstatus Kart" (https://miljostatus.miljodirektoratet.no[2]). Daily river flow rates are estimates from a distributed version of the HBV model provided by the Norwegian Water Resources and Energy Directorate (Beldring et al., 2003).

Best fit linear regression gives $A = 0.40$ and $B = -0.38$, which allows us to estimate TSS from the daily river flow rate, using

$$TSS = e^{-0.38} \cdot F^{0.40} \tag{A.4}$$

The function of TSS estimates and the observed values used to compute the regression constants are plotted in Fig. A.2.
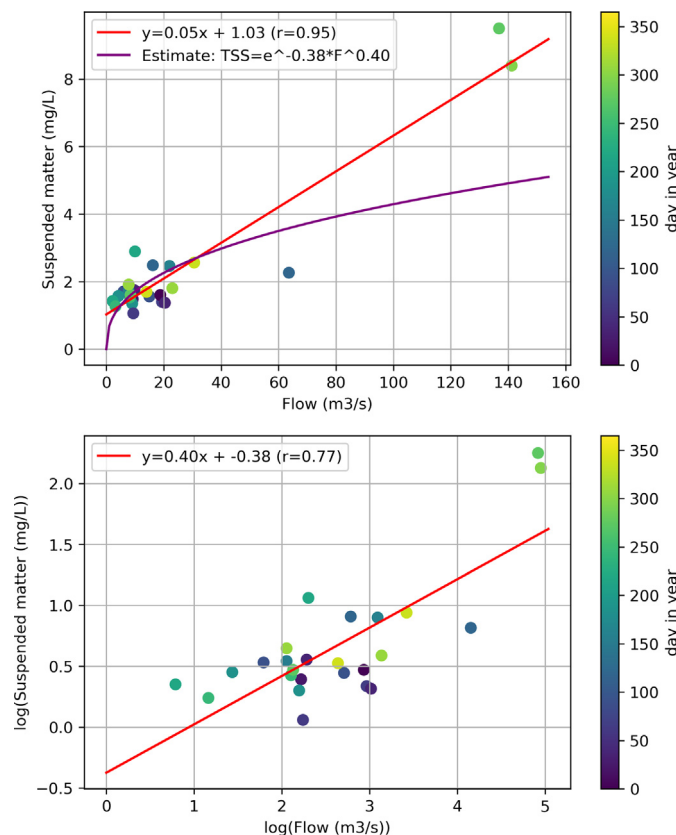

Fig. A.2. Observed TSS as function of river flow rate F, including lines for best fit linear regression.

The concentration of Al associated with particles is assumed to be linearly related to TSS, using a conversion coefficient ϕ

$$C_{PAR} = \phi \cdot TSS \tag{A.5}$$

---

[2] https://vannmiljofaktaark.miljodirektoratet.no/Home/Details/90047?param=TSM&medium=VF medium = VF

Table A.2

Observational data. Specie fractions of total concentration in brackets. River flow is from HBV model.

Date	River flow	total Al	lmm conc	colloid conc	part conc
2008.05.10	16.8	157	35 (22)	82 (52)	40 (25)
2008.05.11	16.0	140	33 (24)	68 (49)	39 (28)
2008.05.12	15.3	148	28 (19)	78 (53)	42 (28)
2008.05.21	11.2	108	10 (9)	64 (59)	34 (31)
2008.05.22	10.7	120	27 (23)	75 (63)	18 (15)
Mean fraction			19	55	26

In our estimates, we used particle-bound Al concentration data from 2008 (Table A.2) to approximate ϕ. Unfortunately, *TSS* measurements taken at equal time were not available, but were estimated from HBV river flow model data (Table A.2) using Eq. (A.4).

Measured particle-bound Al concentration, estimated *TSS* concentration and ratio approximations are shown in Fig. A.3. The mean C_{PAR}/TSS ratio was $17.48 \cdot 10^{-3}$, which is used in our simulations.
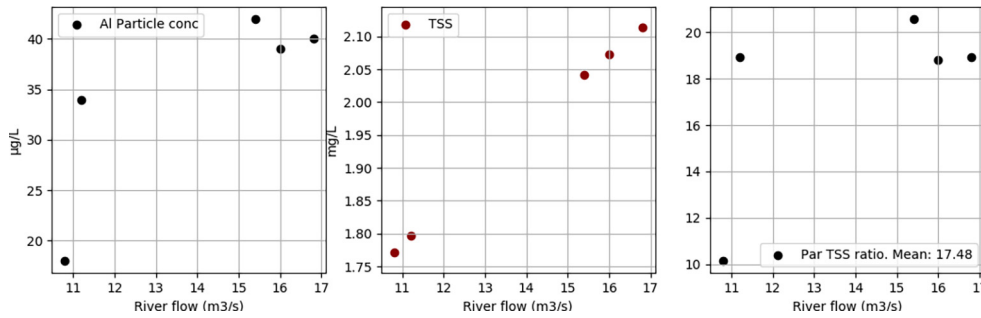

Fig. A.3. Measured particle-bound Al concentration (left), estimated TSS concentration (center) and C_{PAR}/TSS ratio (right).

Now, under the given assumptions, the estimated total Al concentration C_T is the sum of the LMM, humic colloid and particle fractions:

$$C_T = C_{LMM} + C_{COL} + C_{PAR} \tag{A.6}$$

Since the total concentrations vary with time, the final relative fractions of each specie can now be computed from C_T:

$$f_{LMM} = \frac{C_{LMM}}{C_T} \tag{A.7}$$

$$f_{COL} = \frac{C_{COL}}{C_T} \tag{A.8}$$

$$f_{PAR} = \frac{C_{PAR}}{C_T} \tag{A.9}$$

In the model, the total mass of the Al release during the whole simulation period (M_N) can be computed using the total concentration C_T and the river flow rate F from the river model (HBV) at each time step i,

$$M_N = \sum_{i=1,N} \left(C_{T(i)} \cdot F_i \cdot dt \right) \tag{A.10}$$

where dt is the length of each time interval (86,400 s at daily intervals). Seeding a discrete number of numerical units (trajectories), each unit can be interpreted as a 'super-particle', representing a certain amount of Al mass (R), which can be computed by distributing the total mass released (M_N) over a chosen total number of trajectories seeded in the simulation (N_N).

$$R = \frac{M_N}{N_N} \tag{A.11}$$

We assume that the instantaneous Al concentration in the river water in a certain time step can be expressed with the released mass per water volume, as

$$C_{T(i)} = \frac{N_i \cdot R}{F_i \cdot dt} \tag{A.12}$$

where N_i is the total number of trajectories seeded per time step. Hence, the total number of trajectories seeded in each time step (N_i) can be estimated as

$$N_i = \frac{C_{T(i)} \cdot F_i \cdot dt}{R} \tag{A.13}$$

and the number of released trajectories in each specie per time step is

$$N_{LMM(i)} = N_i \cdot f_{LMM(i)} \tag{A.14}$$

$$N_{COL(i)} = N_i \cdot f_{COL(i)} \tag{A.15}$$

$$N_{PAR(i)} = N_i \cdot f_{PAR(i)} \tag{A.16}$$

each rounded to integer numbers.

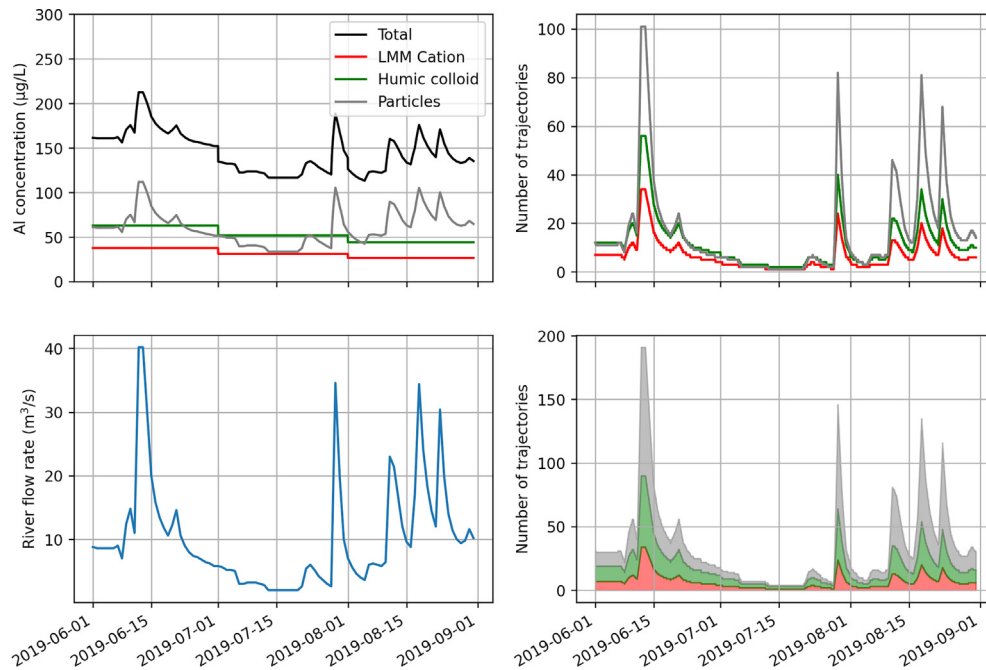An example of such estimate of the river Al run-off is shown in Fig. A.4.

Fig. A.4. Time series of estimated Al concentration in river runoff (upper left) and river flow rate (lower left) for the time period from 2019.06.01 to 2019.09.01, using the method described in the present appendix. Upper right panel shows the number of trajectories of each specie released per hour in the model, while lower right panel shows the total number of trajectories released per hour. Only species LMM cation, humic colloids and particles were released in the model.

Appendix B. Supplementary data

Supplementary data to this article can be found online at https://doi.org/10.1016/j.scitotenv.2023.161399.

References

Albretsen, J., Sperrevik, A.K., Staalstrøm, A., Sandvik, A.D., Vikebø, F., Asplin, L., 2011. NorKyst-800 Report No. 1: User Manual and Technical Descriptions. Fisken og havet URL: doi:10.1007/978-1-4020-4410-6_247.

Arndt, S., Vanderborght, J.P., Regnier, P., 2007. Diatom growth response to physical forcing in a macrotidal estuary: coupling hydrodynamics, sediment transport, and biogeochemistry. J. Geophys. Res. Oceans 112. https://doi.org/10.1029/2006JC003581 URL: 10.1029/2006JC003581.

Artigue, L., Wyatt, N.J., Lacan, F., Mahaffey, C., Lohan, M.C., 2021. The importance of water mass transport and dissolved-particle interactions on the aluminum cycle in the subtropical North Atlantic. Glob. Biogeochem. Cycles, e2020GB006569 https://doi.org/10.1029/2020GB006569 URL: 10.1029/2020GB006569.

Asplin, L., Albretsen, J., Johnsen, I.A., Sandvik, A.D., 2020. The hydrodynamic foundation for salmon lice dispersion modeling along the norwegian coast. Ocean Dyn. 70, 1151–1167. https://doi.org/10.1007/s10236-020-01378-0.

Bars, Y.L., Vallaeys, V., Deleersnijder, E., Hanert, E., Carrere, L., Channelière, C., 2016. Unstructured-mesh modeling of the Congo river-to-sea continuum. Ocean Dyn. 66, 589–603. https://doi.org/10.1007/s10236-016-0939-x URL: 10.1007/s10236-016-0939-.

Beldring, S., Engeland, K., Roald, L.A., Sælthun, N.R., Voksø, A., 2003. Estimation of parameters in a distributed precipitation-runoff model for Norway. URL:Hydrol. Earth Syst. Sci. 7, 304–316. https://doi.org/10.5194/hess-7-304-2003 10.5194.

Chao, Y., Farrara, J.D., Zhang, H., Zhang, Y.J., Ateljevich, E., Chai, F., Davis, C.O., Dugdale, R., Wilkerson, F., 2017. Development, implementation, and validation of a modeling system for the San Francisco Bay and estuary. Estuar. Coast. Shelf Sci. 194, 40–56. https://doi.org/10.1016/j.ecss.2017.06.005 URL: 10.1016/j.ecss.2017.06.005.

Christensen, K.H., Breivik, Øyvind, Dagestad, K.F., Röhrs, J., Ward, B., 2018. Short-term predictions of oceanic drift. Oceanography 31. https://doi.org/10.5670/oceanog.2018.310 URL: 10.5670/oceanog.2018.310.

Crawford, C.G., 1991. Estimation of suspended-sediment rating curves and mean suspended-sediment loads. J. Hydrol. 129, 331–348. https://doi.org/10.1016/0022-1694(91)90057-O URL: 10.1016/0022-1694(91)90057-O.

Dagestad, K.F., Röhrs, J., Breivik, Ø., Ådlandsvik, B., 2018. Opendrift v1.0: a generic framework for trajectory modelling. URL:Geosci. Model Dev. 11, 1405–1420. https://doi.org/10.5194/gmd-11-1405-2018. https://www.geosci-model-dev.net/11/1405/2018/.

Dalsøren, S.B., Albretsen, J., Asplin, L., 2020. New validation method for hydrodynamic fjord models applied in the hardangerfjord, Norway. Estuar. Coast. Shelf Sci. 246, 107028. https://doi.org/10.1016/j.ecss.2020.107028 URL: 10.1016/j.ecss.2020.107028.

Direktoratet for naturforvaltning, 2001. Kalking i vann og vassdrag. DN-Notat 2001-2. Direktoratet for naturforvaltning. In Norwegian with English summary. available from https://www.miljodirektoratet.no/globalassets/publikasjoner/dirnat2/multimedia/48015/vegarsvassdraget.pdf.

Egbert, G.D., Erofeeva, S.Y., 2002. Efficient inverse modeling of barotropic ocean tides. J. Atmos. Ocean. Technol. 19, 183–204. https://doi.org/10.1175/1520-0426(2002)019<0183:EIMOBO>2.0.CO;2 URL: doi:10.1016/j.scitotenv.2019.01.434.

Elskens, M., Gourgue, O., Baeyens, W., Chou, L., Deleersnijder, E., Leermakers, M., de Brauwere, A., 2014. Modelling metal speciation in the scheldt estuary: combining a flexible-resolution transport model with empirical functions. Sci. Total Environ. 476–477, 346–358. https://doi.org/10.1016/j.scitotenv.2013.12.047.

Fairall, C.W., Bradley, E.F., Rogers, D.P., Edson, J.B., Young, G.S., 1996. Bulk parameterization of air-sea fluxes for tropical ocean-global atmosphere coupled-ocean atmosphere response experiment. J. Geophys. Res. Oceans 101, 3747–3764. https://doi.org/10.1029/95JC03205 URL: doi:10.1029/95JC03205.

Ganju, N.K., Brush, M.J., Rashleigh, B., Aretxabaleta, A.L., del Barrio, P., Grear, J.S., Harris, L.A., Lake, S.J., McCardell, G., O'Donnell, J., Ralston, D.K., Signell, R.P., Testa, J.M., Vaudrey, J.M.P., 2016. Progress and challenges in coupled hydrodynamic-ecological estuarine modeling. Estuar. Coasts 39, 311–332. https://doi.org/10.1007/s12237-015-0011-y URL: 10.1007/s12237-015-0011-y.

Haidvogel, D., Arango, H., Budgell, W., Cornuelle, B., Curchitser, E., Lorenzo, E.D., Fennel, K., Geyer, W., Hermann, A., Lanerolle, L., Levin, J., McWilliams, J., Miller, A., Moore, A., Powell, T., Shchepetkin, A., Sherwood, C., Signell, R., Warner, J., Wilkin, J., 2008. Ocean forecasting in terrain-following coordinates: formulation and skill assessment of the Regional Ocean modeling system. J. Comput. Phys. 227, 3595–3624. https://doi.org/10.1016/j.jcp.2007.06.016 URL: 10.1016/j.jcp.2007.06.016.

Hartnett, M., Berry, A., 2012. Numerical modelling of the transport and transformation of trace metals in a highly dynamic estuarine environment. Adv. Eng. Softw. 44, 170–179. https://doi.org/10.1016/j.advengsoft.2011.05.009.

Hobbie, J.E., 2000. Estuarine Science: A Synthetic Approach to Research and Practice. URL:Island Press.

Hydes, D., Liss, P., 1977. The behaviour of dissolved aluminium in estuarine and coastal waters. Estuar. Coast. Mar. Sci. 5, 755–769. https://doi.org/10.1016/0302-3524(77)90047-0 URL: 10.1016/0302-3524(77)90047-0.

Ivanov, E., Capet, A., Barth, A., Delhez, E.J., Soetaert, K., Grégoire, M., 2020. Hydrodynamic variability in the southern bight of the North Sea in response to typical atmospheric and tidal regimes. Benefit of using a high resolution model. Ocean Model. 154, 101682. https://doi.org/10.1016/j.ocemod.2020.101682 URL: 10.1016/j.ocemod.2020.101682.

Jones, C.E., Vicente-Beckett, V., Chapman, J., 2019. Coal mine-affected water releases, turbidity and metal concentrations in the Fitzroy River Basin, Queensland, Australia. Environ. Earth Sci. 78. https://doi.org/10.1007/s12665-019-8734-x URL: doi:10.1007/s12665-019-8734-x.

Kanamitsu, M., DeHaan, L., 2011. The added value index: a new metric to quantify the added value of regional models. J. Geophys. Res. Atmos. 116. https://doi.org/10.1029/2011JD015597 URL: 10.1029/2011JD015597.

Kroglund, F., Høgberget, R., Haraldstad, T., Økland, F., Thorstad, E.B., Teien, H.C., Rosseland, B.O., Salbu, B., Nilsen, T.O., Stefansson, S.O., Guttrup, J., 2011. Are salmon smolts affected by aluminium in estuaries? Results from River Storelva, 2007. NIVA-Report 6245-2011. Norsk institutt for vannforskning. Norwegian with English Summary.

Liu, C., Wang, R., Gao, H., Wu, X., Yin, D., 2022. Transport of trace metals and their bioaccumulation in zooplankton from changjiang (Yangtze River) to the East China Sea. Sci. Total Environ. 851, 158156. https://doi.org/10.1016/j.scitotenv.2022.158156 URL: 10.1016/j.scitotenv.2022.158156.

Lynch, D.R., Greenberg, D.A., Bilgili, A., McGillicuddy Jr., D.J., Manning Jr., J.P., Aretxabaleta Jr., A.L., 2014. Particles in the Coastal Ocean: Theory and Applications. Cambridge University Press.

Machado, A.A.D.S., Spencer, K., Kloas, W., Toffolon, M., Zarfl, C., 2016. Metal fate and effects in estuaries: a review and conceptual model for better understanding of toxicity. Sci. Total Environ. 541, 268–281. https://doi.org/10.1016/j.scitotenv.2015.09.045 URL: doi:10.1016/j.scitotenv.2015.09.045.

Müller, M., Homleid, M., Ivarsson, K.I., Køltzow, M.A.Ø., Lindskog, M., Midtbø, K.H., Andrae, U., Aspelien, T., Berggren, L., Bjørge, D., Dahlgren, P., Kristiansen, J., Randriamampianina, R., Ridal, M., Vignes, O., 2017. AROME-MetCoOp: a nordic convective-scale operational weather prediction model. Weather Forecast. 32, 609–627. https://doi.org/10.1175/WAF-D-16-0099.1 URL: 10.1175/WAF-D-16-0099.1.

Periáñez, R., Elliott, A., 2002. A particle-tracking method for simulating the dispersion of non-conservative radionuclides in coastal waters. J. Environ. Radioact. 58, 13–33. https://doi.org/10.1016/S0265-931X(01)00028-5 URL: 10.1016/S0265-931X(01)00028-5.

Resing, J.A., Sedwick, P.N., German, C.R., Jenkins, W.J., Moffett, J.W., Sohst, B.M., Tagliabue, A., 2015. Basin-scale transport of hydrothermal dissolved metals across the South Pacific Ocean. Nature 523, 200–203. https://doi.org/10.1038/nature14577 URL: 10.1038/nature14577.

Salbu, B., 2016. Environmental impact and risk assessments and key factors contributing to the overall uncertainties. J. Environ. Radioact. 151, 352–360. https://doi.org/10.1016/j.jenvrad.2015.09.001 URL: 10.1016/j.jenvrad.2015.09.001.

Sandvik, A.D., Skagseth, Øystein, Skogen, M.D., 2016. Model validation: issues regarding comparisons of point measurements and high-resolution modeling results. Ocean

Model. 106, 68–73. https://doi.org/10.1016/j.ocemod.2016.09.007 URL: 10.1016/j.ocemod.2016.09.007.

Shchepetkin, A.F., McWilliams, J.C., 2005. The regional oceanic modeling system (ROMS): a split-explicit, free-surface, topography-following-coordinate oceanic model. Ocean Model. 9, 347–404. https://doi.org/10.1016/j.ocemod.2004.08.002 URL: 10.1016/j.ocemod.2004.08.002.

Simonsen, M., Lind, O.C., Saetra, Ø., Isachsen, P.E., Teien, H.C., Albretsen, J., Salbu, B., 2019a. Coastal transport of river-discharged radionuclides: impact of speciation and transformation processes in numerical model simulations. Sci. Total Environ. 669, 856–871. https://doi.org/10.1016/j.scitotenv.2019.01.434 URL: doi:10.1016/j.scitotenv.2019.01.434.

Simonsen, M., Teien, H.C., Lind, O.C., Saetra, Ø., Albretsen, J., Salbu, B., 2019b. Modeling key processes affecting Al speciation and transport in estuaries. Sci. Total Environ. 687, 1147–1163. https://doi.org/10.1016/j.scitotenv.2019.05.318 URL: doi:10.1016/j.scitotenv.2019.05.318.

Stigebrandt, A., 2012. Hydrodynamics and Circulation of Fjords. Springer Netherlands, Dordrecht, pp. 327–344 https://doi.org/10.1007/978-1-4020-4410-6_247 URL: doi:10.1007/978-1-4020-4410-6_247.

Syvitski, J.P., Burrell, D.C., Skei, J.M., 1987. Fjords: Processes and Products. Springer-Verlag, New York https://doi.org/10.1007/978-1-4612-4632-9.

Sætre, R., 2007. The Norwegian Coastal Current – Oceanography and Climate. Tapir Acad, Trondheim, Norway.

Teien, H.C., Salbu, B., Kroglund, F., Rosseland, B.O., 2004. Transformation of positively charged aluminium-species in unstable mixing zones following liming. Sci. Total Environ. 330, 217–232. https://doi.org/10.1016/j.scitotenv.2004.03.040 URL: 10.1016/j.scitotenv.2004.03.040.

Teien, H.C., Standring, W.J., Salbu, B., 2006. Mobilization of river transported colloidal aluminium upon mixing with seawater and subsequent deposition in fish gills. Sci. Total Environ. 364, 149–164. https://doi.org/10.1016/j.scitotenv.2006.01.005 URL: 10.1016/j.scitotenv.2006.01.005.

Tipping, E., Lofts, S., Stockdale, A., 2016. Metal speciation from stream to open ocean: modelling v. measurement. Environ. Chem. 13, 464–477. https://doi.org/10.1071/EN15111 URL: 10.1071/EN15111.

Umlauf, L., Burchard, H., 2003. A generic length-scale equation for geophysical turbulence models. J. Mar. Res. 61, 235–265. https://doi.org/10.1357/002224003322005087 URL: 10.1357/002224003322005087.

Upadhyay, S., 2008. Sorption model for dissolved and particulate aluminium in the Conway estuary, UK. Estuar. Coast. Shelf Sci. 76, 914–919. https://doi.org/10.1016/j.ecss.2007.08.021 URL: 10.1016/j.ecss.2007.08.021.

Vallaeys, V., Lambrechts, J., Delandmeter, P., PÃ¤tsch, J., Spitzy, A., Hanert, E., Deleersnijder, E., 2021. Understanding the circulation in the deep, micro-tidal and strongly stratified Congo River estuary. Ocean Model. 167, 101890. https://doi.org/10.1016/j.ocemod.2021.101890 URL: 10.1016/j.ocemod.2021.101890.

Wang, Z.W., Ren, J.L., Zhang, G.L., Liu, S.M., Zhang, X.Z., Liu, Z., Zhang, J., 2015. Behavior of dissolved aluminum in the huanghe (Yellow River) and its estuary: impact of human activities and sorption processes. Estuar. Coast. Shelf Sci. 153, 86–95. https://doi.org/10.1016/j.ecss.2014.12.010 URL: 10.1016/j.ecss.2014.12.010.

Xu, H., Weber, T., 2021. Ocean dust deposition rates constrained in a data-assimilation model of the marine aluminum cycle. Glob. Biogeochem. Cycles 35, e2021GB007049. https://doi.org/10.1029/2021GB007049 URL: 10.1029/2021GB007049.

Yang, Z., Khangaonkar, T., 2009. Modeling tidal circulation and stratification in Skagit River estuary using an unstructured grid ocean model. Ocean Model. 28, 34–49. https://doi.org/10.1016/j.ocemod.2008.07.004 URL: 10.1016/j.ocemod.2008.07.004.

Zhao, L., Chen, C., Vallino, J., Hopkinson, C., Beardsley, R.C., Lin, H., Lerczak, J., 2010. Wetland-estuarine-shelf interactions in the Plum Island sound and Merrimack River in the Massachusetts coast. J. Geophys. Res. Oceans 115. https://doi.org/10.1029/2009JC006085 URL: 10.1029/2009JC006085.

Zhou, F., Chai, F., Huang, D., Xue, H., Chen, J., Xiu, P., Xuan, J., Li, J., Zeng, D., Ni, X., Wang, K., 2017. Investigation of hypoxia off the changjiang estuary using a coupled model of ROMS-CoSiNE. Prog. Oceanogr. 159, 237–254. https://doi.org/10.1016/j.pocean.2017.10.008 URL: 10.1016/j.pocean.2017.10.008.